

Hybrid-MPET: an open-source simulation software for hybrid electrode batteries

Qiaohao Liang¹ and **Martin Z. Bazant^{2,3,*}**

¹Department of Materials Science and Engineering, Massachusetts Institute of Technology,
Cambridge, MA 02139 USA

²Department of Chemical Engineering, Massachusetts Institute of Technology, Cambridge,
MA 02139 USA

³Department of Mathematics, Massachusetts Institute of Technology, Cambridge, MA 02139
USA

*Corresponding author: bazant@mit.edu

May 26, 2023

Abstract

As the design of single-component battery electrodes has matured, the battery industry has turned to hybrid electrodes with blends of two or more active materials to enhance battery performance. Leveraging the best properties of each material while mitigating their drawbacks, multi-component hybrid electrodes open a vast new design space that could be most efficiently explored through simulations. In this article, we introduce a mathematical modeling framework and open-source battery simulation software package for Hybrid Multiphase Porous Electrode Theory (Hybrid-MPET), capable of accounting for the parallel reactions, phase transformations and multiscale heterogeneities in hybrid porous electrodes. Hybrid-MPET models can simulate both solid solution and multiphase active materials in hybrid electrodes at intra-particle and inter-particle scales. Its modular design also allows the combination of different active materials at any capacity fraction. To illustrate the novel features of Hybrid-MPET, we present experimentally validated models of silicon-graphite (Si-Gr) anodes used in electric vehicle batteries and carbon monofluoride (CF_x) - silver vanadium oxide (SVO) cathodes used in implantable medical device batteries. The results demonstrate the potential of Hybrid-MPET models to accelerate the development

of hybrid electrode batteries by providing fast predictions of their performance over a wide range of design parameters and operating protocols.

Introduction

Over the past 30 years, lithium-ion batteries have become the ubiquitous power source for portable electronics and electric vehicles [1–3]. As the next-generation applications demand further enhanced battery performance, battery research has been focused on developing new cathode and anode materials to meet the growing demand for improvements in energy and power density, high-rate performance, cycle stability, environmental friendliness, and production costs [4, 5]. It is of great scientific and practical significance for batteries today to be tailored towards the particular needs of the applications, where the performance of specialized batteries is often tuned through the use of different porous cathode and anode materials [6]. However, most widely used intercalation-based single material electrodes such as the layered transition-metal oxide $\text{LiNi}_{1-x-y}\text{Co}_x\text{Mn}_y\text{O}_2$ (NMC) cathode [7–10], $\text{LiNi}_{1-x-y}\text{Co}_x\text{Al}_y\text{O}_2$ (NCA) cathode [7, 11, 12], LiFePO_4 (LFP) [13, 14] cathode and graphite anode [15–17] are rapidly reaching their theoretical limits and have difficulties to meet all the required performance metrics at the same time.

To overcome the inherent limitations of single-component electrodes, researchers are increasingly focusing on developing hybrid electrodes [18–40], in which multiple active electrode materials can combine their merits to achieve better battery performances. A hybrid porous electrode is most commonly comprised of a uniform physical mixture of two or more distinct types of particles, each containing different active materials that independently react with Li^+ , typically through intercalation or conversion types mechanisms during battery cycling. For example, the silicon-graphite hybrid porous anode [24–28, 30] introduces small amounts of high energy density silicon particles (3579 mAh/g for $\text{Li}_{15}\text{Si}_4$) [41, 42] into the graphite electrode (372 mAh/g for LiC_6) to considerably increase its specific capacity. A hybrid porous electrode can also contain particles that leverage multiple parallel lithiation reactions to improve electrode performance. For example, in lithium primary batteries used to power pacemakers and implantable cardioverter-defibrillators (ICDs) [19–23], the carbon monofluoride (CF_x) - silver vanadium oxide $\text{Ag}_2\text{V}_4\text{O}_{11}$ (SVO) hybrid porous cathode takes advantage of both the high rate capability of SVO and the great specific capacity of CF_x , allowing these batteries to discharge at low currents ($\sim \mu\text{A}$) for years without replacement and provide pulse currents ($\sim 3\text{A}$) on demand. In SVO particles, the fast reduction reaction from V^{5+} can support high current pulses, while the slower Ag^+ displacement reaction improves both the energy density and the electronic conductivity of the cathode [22, 43–45]. Note that other energy storage devices have also adopted the technique of blending multiple active materials to create high-performance hybrid electrodes: hybrid nanostructured materials that combine

carbon based materials with pseudocapacitive metal oxides have been used to achieve high-performance electrochemical capacitors [46, 47].

The increasing popularity of hybrid porous electrodes has led to a growing demand for improved battery simulation software capable of accounting for both the parallel reactions from individual active materials, phase transformations and multiscale heterogeneities [17, 48–57] in hybrid porous electrodes. However, existing open-source battery simulation software [58–61] based on Porous Electrode Theory (PET) framework [48, 62–66] cannot meet these requirements without significant modification of their software code by the users. In this article, we introduce a mathematical modeling framework and open-source battery simulation software package for Hybrid Multiphase Porous Electrode Theory (Hybrid-MPET). Building upon volume averaging methods and microscopic electrochemical relations from PET [62–66], as well as the nonequilibrium thermodynamics [50, 57, 67–73] in Multiphase Porous Electrode Theory (MPET) [48], Hybrid-MPET models are capable of accurately simulating both solid solution and multiphase active materials in the hybrid porous electrode at intra-particle and inter-particle scales. The capacity fractions, thermodynamic, kinetic, and transport properties of different active materials can also easily be adjusted due to the modular implementation of Hybrid-MPET. We encourage reuse and modification of Hybrid-MPET, and we hope that it can serve as open-source simulation platform to aid investigation of new hybrid electrode chemistries together with experimental validation.

The paper is organized by the following sections. In the Methods section, we describe how Hybrid-MPET addresses parallel reactions at intra-particle and inter-particle scale in greater detail. In the Results section, we highlight the novel features of our Hybrid-MPET through sample case studies: Hybrid-MPET models are validated against experimental data from the silicon-graphite hybrid porous anode, SVO, and CF_x - SVO hybrid porous cathode. We conclude with a summary and an outlook for future research developments in the Conclusion section.

Methods

The main goal of the Hybrid-MPET is to create an open-source battery simulation software capable of accurately simulating the performance of hybrid electrode batteries. Hybrid-MPET falls into the category of electrochemical pseudo-two-dimensional (P2D) model, and thus utilizes the same volume averaging methods and preserves the fundamental microscopic electrochemical relations from Porous Electrode Theory (PET) [62–66], including conservation of mass and charge in solid phase, liquid phases, and across interfaces. Among the existing open-source battery simulation software [48, 58–61], we build Hybrid-MPET by adapting Multiphase Porous Electrode Theory (MPET) [48] for hybrid porous electrode simulations.

We chose to heavily reference MPET because it can accommodate both classical PET models for solid solution active materials and models for multiphase active materials based on nonequilibrium thermodynamics [50, 57, 67–73] in the same framework. Many commercially successful hybrid porous electrodes often contain both phase separating and solid solution materials, and we seek to select the most accurate and suitable method to describe the thermodynamics of each active material from the following two options. We could take the classical PET approach and describe thermodynamics of active materials by fitting the open circuit voltage (OCV) as a function of state of charge, which will be only accurate for solid solution active materials [48, 50, 57, 67–69, 74] with Fickian diffusion. For phase separating active materials such as LFP [13, 14] and graphite [15–17], often characterized by voltage plateaus in their OCV, they have multiple stable phases of different equilibrium concentrations, and such complex thermodynamic behavior cannot be described by PET models despite additional empirical modifications [75, 76]. Instead, for these materials, MPET and Hybrid-MPET treats their OCVs as emergent properties of multiphase materials that reflects phase separation. We can thus describe the thermodynamics of phase separating materials through phase field [77, 78] models adapted for electrochemical systems [49, 50, 57, 67–70, 79, 80], where the OCV is derived from the free energy function and diffusional chemical potential [74] of inserted Li^+ in the active material. Free energy is a function of concentration and gradients of concentration, where common tangent lines can be constructed under to represent pathway for the material to lower its energy by phase separating. Taking into account nonequilibrium thermodynamics, MPET has thus been able to predict reaction heterogeneities in multiphase porous electrodes [17, 51–53, 57, 68, 81]. Such heterogeneities are experimentally observed to be highly dependent on applied current [49, 52, 57, 81] yet often lost over intermediate length scales as a result of volume averaging and could lead to simulation inaccuracies [48]. By referencing MPET, Hybrid-MPET is expected to also capture evolution of reaction heterogeneity across simulated particles in hybrid porous electrodes, which is further complicated by the existence of parallel reactions. Hybrid-MPET thus distinguishes itself from MPET [48] and other existing open-source battery simulation software [58–61] by its ability to simulate hybrid porous electrodes with multiple active materials. We briefly revisit how reactions at particle scale are connected to macroscopic current in MPET for single material porous electrodes, and show how Hybrid-MPET introduces new equations to account for parallel reactions from different active electrode materials at intra-particle and inter-particle scale.

In MPET, each of the N finite volumes across the thickness L of the porous electrode hosts P active particles. For particle p in finite volume n , $\bar{c}_{n,p} \in [0, 1]$ is used to describe its average state of charge (SOC). For intercalation reactions, SOC is known as filling fraction or a dimensionless Li^+ concentration in solid phase hosts; for primary batteries, SOC is often interchangeably used with depth of discharge or battery utilization. For non-homogeneous particles, c is tracked at each discretization layer depth in the particle [48]

to observe the effects of solid diffusion, which can be used together to reconstructed \bar{c} for the whole particle. For particle p in finite volume n , its reaction takes place independently from that of other particles, and is quantified by average volumetric reaction rate $\frac{\partial \bar{c}_{n,p}}{\partial t}$. The sum of reactions from all particles in finite volume n yields its total volume averaged reaction rate R_n^V . The integral of the net charge consumed by the reactions across the finite volumes in the electrode will yield the macroscopic current density i_{cell} . Reproduced from Eq. 58-60 from MPET [48] and simplified by assuming Li^+ as the only cation species in lithium-ion batteries, $\frac{\partial \bar{c}_{n,p}}{\partial t}$, R_n^V , and i_{cell} (for both anode and cathode) are defined in Eq. 1 - 3, respectively:

$$\frac{\partial \bar{c}_{n,p}}{\partial t} = \frac{1}{V_{n,p}} \int_{A_{n,p}} j_{n,p} dA \quad (1)$$

$$R_n^V = -(1 - \epsilon) P_L \sum_{p=1}^P \tilde{V}_{n,p} \frac{\partial \bar{c}_{n,p}}{\partial t} \quad p = 1, 2, \dots, P \quad (2)$$

$$i_{cell} = \sum_{n_a=1}^{N_a} e R_{n_a}^V \frac{L_a}{N_a} = - \sum_{n_c=1}^{N_c} e R_{n_c}^V \frac{L_c}{N_c} \quad n = 1, 2, \dots, N \quad (3)$$

where $j_{n,p}$ is the reaction flux from particle n in finite volume p and is equal to the net reduction current density $i_{n,p}$ scaled by (de)lithiation reaction stoichiometry. ϵ is the porosity of the electrode, P_L is the loading percent of active material in solid phase of the electrode, which are both electrode scale parameters. $\tilde{V}_{n,p} = \frac{V_{n,p}}{\sum_{p=1}^P V_{n,p}}$ is the fraction between volume of particle p and total volume of particles in finite volume n .

In Fig. 1, we show a comparison between single-component electrodes and hybrid electrodes from a model formulation perspective. The complexities introduced by multiple active components and particle types mostly occur at the particle scale, and thus modifications needed for parallel reactions at intra-particle and inter-particle scale take place in Eq. 1 - 2. The total reaction rate R_n^V will be reconstructed when there are multiple active components and particle types in volume n . In greater detail, at intra-particle scale, we will define average state of charge $\bar{c}_{n,p}$ for a "hybrid" particle with multiple active components; at inter-particle scale, we also introduce volume correction terms to simulate hybrid electrodes made up of different active particles with any given capacity fraction. Eq. 3 as well as other conservation of charge and mass equations in MPET are kept unchanged for both cases below.

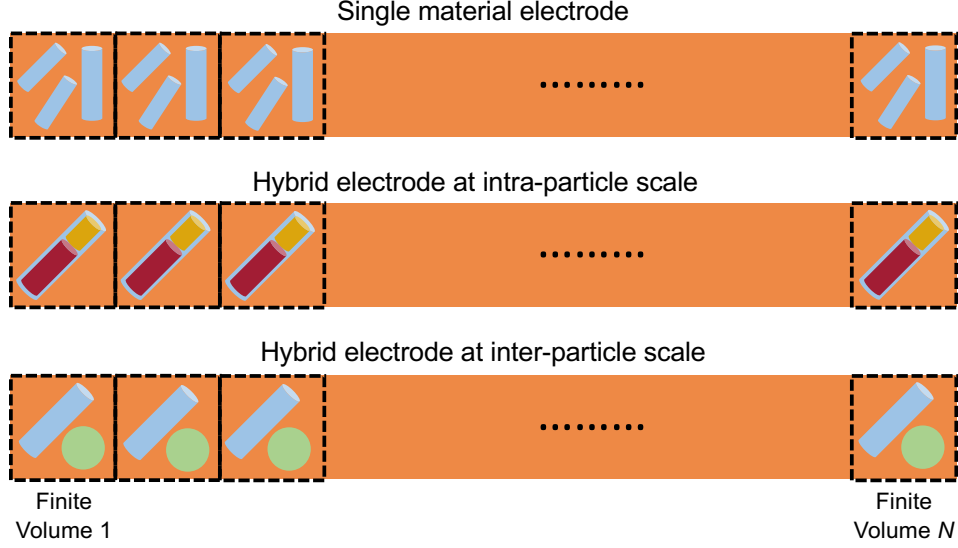


Figure 1: Schematic drawing of finite volume discretization of porous electrodes across their thickness. For single material electrodes, all particles contain the same active material. For a hybrid electrode, at intra-particle scale, each of its particles may have multiple active components; at inter-particle scale, each of its finite volume may have different particle types.

Intra-particle scale parallel reactions

In Hybrid-MPET, simulation of intra-particle parallel reactions is crucial when modeling a hybrid electrode made up of single-type particles that allow multiple reactions. The overall reaction rate in such a "hybrid" particle takes contributions from all active components, which coexist inside the particle's volume. Within particle p in finite volume n , M different active components coexist and share the same the particle volume $V_{n,p}$ and active reaction area $A_{n,p}$. The active components have theoretical volume capacity $\rho_1, \rho_2, \dots, \rho_M$, and their normalized fractions are constrained by $\sum_{m=1}^M \tilde{\rho}_m = 1$. Within particle p in finite volume n , we track the state of charge of each active component separately $\bar{c}_{n,p,1}, \bar{c}_{n,p,2}, \dots, \bar{c}_{n,p,M}$ and thus

$$\bar{c}_{n,p} = \sum_{m=1}^M \tilde{\rho}_m \bar{c}_{n,p,m} \quad m = 1, 2, \dots, M \quad (4)$$

$$\bar{c}_n = \frac{\sum_{p=1}^P V_{n,p} \bar{c}_{n,p}}{\sum_{p=1}^P V_{n,p}} \quad (5)$$

Since the electrode was discretized into finite volumes of equal size, the macroscopic electrode average state of charge will just be the average of $\bar{c}_1, \bar{c}_2, \dots, \bar{c}_N$, which is equivalent to Eq. 63 in MPET [48]. Building upon

Eq. 4, the volumetric reaction rate from Eq. 1 is modified to,

$$\frac{\partial \bar{c}_{n,p}}{\partial t} = \frac{\partial(\sum_{m=1}^M \tilde{\rho}_m \bar{c}_{n,p,m})}{\partial t} = \sum_{m=1}^M \left(\tilde{\rho}_m \frac{\partial \bar{c}_{n,p,m}}{\partial t} \right) = \frac{1}{V_{n,p}} \sum_{m=1}^M \left(\tilde{\rho}_m \int_{A_{n,p}} j_{n,p,m} dA \right) \quad (6)$$

where the capacity weighted sum of parallel reactions rates from all M active components yields the average volumetric reaction rate. The reactions are typically described by Butler-Volmer (BV) kinetics [67, 82–86] (assuming only single electron reactions)

$$i_{n,p,m} = j_{n,p,m} e = i_m(k_m, c_{n,p,m}, c_n^l) \left[\exp \left(-\frac{\alpha_m e \eta_{n,p,m}^{\text{eff}}}{k_B T} \right) - \exp \left(\frac{(1 - \alpha_m) e \eta_{n,p,m}^{\text{eff}}}{k_B T} \right) \right] \quad (7)$$

$$\eta_{n,p,m}^{\text{eff}} = \eta_{n,p,m} + i_{n,p,m} R_{film,m} = \Delta \phi_n^s - \Delta \phi_m^{eq}(c_{n,p,m}) + i_{n,p,m} R_{film,m} \quad (8)$$

where exchange current density i_m is a function of rate constant k_m , symmetry coefficient α_m , and Li^+ filling fractions $c_{n,p,m}$ in solid particles and Li^+ concentrations in c_n^l liquid electrolyte. The overpotential $\eta_{n,p,m}$ experienced by active component m within particle p in finite volume n is the difference between electrode potential $\Delta \phi_n^s$ at finite volume n and the equilibrium potential $\Delta \phi_m^{eq}(c_{n,p,m})$ (i.e. open-circuit voltage) of the active material m within particle p , and we can get effective overpotential $\eta_{n,p,m}^{\text{eff}}$ after accounting for film resistance $R_{film,m}$. For each particle p in the same finite volume n , its M active components experience the same $\Delta \phi_n$ and are in contact with electrolyte with concentration c_n^l . For active component m , its reaction rate is determined by material specific k_m , α_m , $\Delta \phi_m^{eq}$, $R_{film,m}$ and particle specific $c_{n,p,m}$. We have now effectively separated M parallel reactions at the intra-particle scale, and therefore the total reaction rate in finite volume n from Eq. 2 is modified to,

$$R_n^V = -(1 - \epsilon) P_L \sum_{p=1}^P \tilde{V}_{n,p} \left(\sum_{m=1}^M \tilde{\rho}_m \frac{\partial \bar{c}_{n,p,m}}{\partial t} \right) \quad (9)$$

where again $\tilde{V}_{n,p} = \frac{V_{n,p}}{\sum_{p=1}^P V_{n,p}}$ is volume fraction of particle p in finite volume n . Instead of solving for $\bar{c}_{n,p}$ directly, we would just be solving for each $\bar{c}_{n,p,m}$ as well as $\Delta \phi_n^s$, $\Delta \phi_n^l$, c_n^l at each finite volume n ; $\bar{c}_{n,p}$ is later reconstructed from Eq. 4.

Inter-particle scale parallel reactions

In Hybrid-MPET, simulation of inter-particle parallel reactions is even more important because most hybrid electrodes are comprised of a uniform physical mixture of two or more distinct types of particles. Let there

be $W \geq 2$ different types of particles in the hybrid porous electrode, which have theoretical volume capacity $\rho_1, \rho_2, \dots, \rho_W$, respectively. We separate the thickness L of the hybrid porous electrode into N finite volumes, each of which hosts P_1 particles of material type 1, P_2 particles of material type 2, ..., and P_W particles of material type W . Then the capacity fraction occupied by type w particles in finite volume n is,

$$\tilde{Q}_w = \tilde{Q}_{n,w} = \frac{Q_{n,w}}{\sum_{w=1}^W Q_{n,w}} = \frac{\sum_{p_w=1}^{P_w} \rho_w V_{n,p_w}}{\sum_{w=1}^W \left(\sum_{p_w=1}^{P_w} \rho_w V_{n,p_w} \right)} \quad w = 1, 2, \dots, W \quad (10)$$

The above setup is limited by the fact that P_1, P_2, \dots, P_W have to be all finite and positive integers $\{P_w \in \mathbb{Z}^+ | w = 1, 2, \dots, W\}$. For type w particles, once their sizes and theoretical volume capacity are set, often through experimental characterization or from literature documents, the capacity fraction of type w active component is only dependent on its number of simulated particles P_w . To simulate hybrid porous electrodes with any given capacity fractions $\tilde{Q}_1^*, \tilde{Q}_2^*, \dots, \tilde{Q}_W^*$ in the electrode, we need to find P_1, P_2, \dots, P_W through solving the set of w equations based on Eq. 10, and obtain the following real number ratios,

$$\frac{P_w}{P_1} = \lambda_{w1} \quad \{\lambda_{w1} \in \mathbb{R}^+ | w = 2, 3, \dots, W\} \quad (11)$$

The most straightforward solution is to use a very large positive integer P_1 to also recover P_2, \dots, P_W as positive integers. Such large values for P_1, P_2, \dots, P_W way exceeds the number of particles necessary to capture evolution of multiscale heterogeneity or population dynamics [10, 48, 50, 57, 87] in porous electrodes. Most of the computational power would be wasted to repeatedly solve extremely similar equations for different particles of the same type in the same finite volume. A single simulation would take days if not weeks to finish, significantly limiting the efficiency in predicting the performance of hybrid porous electrodes.

To overcome this limitation, we introduce volume correction terms at inter-particle scale to simulate hybrid porous electrodes made up of different active particles with target capacity fractions $\tilde{Q}_1^*, \tilde{Q}_2^*, \dots, \tilde{Q}_W^*$ in the electrode. In the finite volume n , the volume correction terms $f_{n,w}$ will scale the volume of type w particles so that capacity fraction $\tilde{Q}_{n,w}^{corr}$ matches \tilde{Q}_w^* ,

$$\tilde{Q}_w^* = \tilde{Q}_{n,w}^{corr} = \frac{Q_{n,w}^{corr}}{\sum_{w=1}^W Q_{n,w}^{corr}} = \frac{\sum_{p_w=1}^{P_w} \rho_w V_{n,p_w} f_{n,w}}{\sum_{w=1}^W \left(\sum_{p_w=1}^{P_w} \rho_w V_{n,p_w} f_{n,w} \right)} \quad w = 1, 2, \dots, W \quad (12)$$

$f_{n,1}, f_{n,2}, \dots, f_{n,W} \in \mathbb{R}^+$ are directly obtained by solving the set of w equations based on Eq. 12. Each finite volume having the correct capacity fraction ensures that the correct capacity fraction is preserved for the hybrid porous electrode at the macroscopic scale. We still track the average SOC in each active particle separately, $\bar{c}_{n,p_w} \in [0, 1]$, which now reflects the average SOC in type w particles we would expect to get

when type w particles have the correct capacity fraction in finite volume n . As the volumes of type w particles are weighted $f_{n,w}$, the average state of charge in volume n becomes,

$$\bar{c}_n^{corr} = \frac{\sum_{w=1}^W \left(\sum_{p_w=1}^{P_w} \rho_w V_{n,p_w} f_{n,w} \bar{c}_{n,p_w} \right)}{\sum_{w=1}^W \left(\sum_{p_w=1}^{P_w} \rho_w V_{n,p_w} f_{n,w} \right)} \quad (13)$$

In finite volume n , a Hybrid-MPET model is numerically still simulating the reactions of P_1 particles of type 1, P_2 particles of type 2, ..., and P_W particles of type W , but we re-scale their contributions to the average state of charge and total reaction rate in finite volume through volume correction. As a result, we can simulate the performance of a hybrid porous electrode with any given capacity fraction. We can also still capture evolution of reaction heterogeneity and population dynamics for any particle type w , as long as we select P_w to be large enough to observe such effects while small enough to finish the simulation in reasonable timescales. Again, in the same finite volume n , all W different types of particles experience the same $\Delta\phi_n^s$ and are in contact with electrolyte with concentration c_n^l . For single electron reactions described by BV kinetics, they are dependent on material type specific k_w , α_w , $\Delta\phi_w^{eq}(c_{n,p_w})$, $R_{film,w}$ and particle specific c_{n,p_w} ,

$$i_{n,p_w} = j_{n,p_w} e = i_w(k_w, c_{n,p_w}, c_n^l) \left[\exp\left(-\frac{\alpha_w e \eta_{n,p_w}^{eff}}{k_B T}\right) - \exp\left(\frac{(1-\alpha_w) e \eta_{n,p_w}^{eff}}{k_B T}\right) \right] \quad (14)$$

$$\eta_{n,p_w}^{eff} = \eta_{n,p_w} + i_{n,p_w} R_{film,w} = \Delta\phi_n^s - \Delta\phi_w^{eq}(c_{n,p_w}) + i_{n,p_w} R_{film,w} \quad (15)$$

The volumetric reaction rate for particles in finite volume n is kept the same as in Eq. 1 because volume correction is numerically applied in the total reaction rate in finite volume n , which now takes contribution from all W types of particles,

$$R_n^{V,corr} = -(1-\epsilon)P_L \sum_{w=1}^W \sum_{p_w=1}^{P_w} \tilde{V}_{n,p_w}^{corr} \frac{\partial \bar{c}_{n,p_w}}{\partial t} \quad (16)$$

where the corrected volume fractions are,

$$\tilde{V}_{n,p_w}^{corr} = \frac{V_{n,p_w} f_{n,w}}{\sum_{w=1}^W \sum_{p_w=1}^{P_w} V_{n,p_w} f_{n,w}} \quad (17)$$

At each time step during the simulation on the side of this hybrid porous electrode, the solutions for \bar{c}_{n,p_w} , $\Delta\phi_n^s$, $\Delta\phi_n^l$, c_n^l will reflect the impact of volume correction terms while simultaneously preserving conservation of charge and mass.

Note that the equations for intra-particle scale and inter-particle scale reactions are consistent with each other. In most cases, a hybrid porous electrode consists of multiple type of particles, each type clearly distinguished by its unique single active component, and thus only the inter-particle scale equations Eq. 12 - 16 are needed. The most common example would be the silicon-graphite hybrid anode [24–28, 30]. Occasionally, some hybrid porous electrodes contain particles with multiple active components, leading to parallel reactions at the intra-particle scale. An example would be carbon monofluoride (CF_x) - silver vanadium oxide (SVO) hybrid cathode [19, 21–23, 43–45], which has both inter-particle scale parallel reactions from CF_x and SVO particles, and intra-particle scale parallel reduction of V^{5+} and Ag^+ in SVO. In this case, we would only need to replace $\bar{c}_{n,pw}$ in Eq. 13 with its expression in Eq. 4 and $\frac{\partial \bar{c}_{n,pw}}{\partial t}$ in Eq. 16 with its expression in Eq. 6.

Results: Experimental validation of Hybrid-MPET models

In this section, we demonstrate example uses of Hybrid-MPET and the predictive power of its models on hybrid porous electrodes batteries from established industrial products. The governing equations and simulation parameters are reported in Appendix A, B, and C.

Silicon-graphite hybrid porous electrode

A silicon-graphite (Si-Gr) hybrid porous electrode is typically used as the anode in rechargeable batteries powering electric vehicles [24–28, 30]. Particles of silicon or silicon oxides are uniform mixed with graphite particles to create a hybrid electrode with good cycle stability from graphite and improved energy density from introduction of silicon. Both silicon ($\text{Li}_{15}\text{Si}_4$) and graphite (LiC_6) take advantage of intercalation reactions and undergo multiple steps of phase separation. Graphite can form many stable phases, as evident in the multiple voltage plateaus in its OCV with increased lithiation [17, 50, 88–90]. Silicon undergoes even more complex phase transformation behaviour during Li^+ de(lithiation), which are accompanied by transition between crystalline and amorphous phases, and significant volume change [30, 91, 92]. Depending on operation history, the phase and volume change of silicon lead to different stress states and give rise to its characteristic OCV hysteresis [93–95] as seen in Fig. 2. We recognize that complex phase-field models coupled with elasto-plastic deformation have been developed for silicon and graphite [80, 96], but integrating them into the Hybrid-MPET models is beyond the scope this work. As a result, the following assumptions are used for simplicity purposes: (a) the fraction of silicon in the Si-Gr electrode is small enough such that the volume changes of silicon particles have negligible impact on electrode parameters and performance [97–100]. (b) silicon stays amorphous and is treated as a solid solution material with fast diffusion. (c) under the relatively low current rates below, other ohmic and transport resistances are negligible. In the future, we encourage the

use of Hybrid-MPET to study interaction between the silicon and graphite at different current rates and include more accurate chemo-mechanical models to capture the multiphase behavior and stress states in silicon.

We first benchmark a Hybrid-MPET model of a Si-Gr electrode against experimental data at room temperature. The Si-Gr electrode was extracted [24] from the anode of the commercial LG M50 21700 cell, and tested in a half-cell setup. In our simulation, we use an estimated 1% silicon mass fraction [101, 102], which is equivalent to silicon accounting for 8.6% of the capacity fraction. We simulate a half-cell with Si-Gr electrode as the cathode, and a lithium foil counter-electrode with fast kinetics as the anode, with a generic separator in between. For reaction kinetics, classical BV kinetics for intercalation reactions are used for both silicon and graphite, whose exchange-current densities vary with both electrolyte and solid concentrations. For electrolyte transport, we use a concentrated Stefan Maxwell electrolyte model to represent a typical 1M LiPF₆ carbonate based electrolyte in lithium-ion batteries. For thermodynamics, we adapt the simplified one-parameter Cahn-Hilliard phase field model [17, 103] to capture the multiphase behavior of graphite. The formulated free energy model with three local minima [103] yields an open-circuit voltage that matches the sloping voltage at low graphite state of charge as well as the stage transitions of voltage at higher graphite state of charge. We resolve silicon’s voltage hysteresis by using two separate OCVs for lithiation and delithiation [30] of amorphous silicon and treat it as a solid solution material. The corresponding OCVs $\Delta\phi_{\text{Gr}}^{eq}$, $\Delta\phi_{\text{Si,Li}}^{eq}$, $\Delta\phi_{\text{Si,Deli}}^{eq}$ can be seen in Fig. 2. We discretize the Si-Gr electrode into 10 finite volumes, each containing 1 spherical silicon particle and 1 spherical graphite particle. For most geometric and physical properties of the cell, electrode, and particles, we directly use the experimentally measured [24] values, and only refit reaction rate constants and Bruggeman exponent for better alignment between simulation and experimental data. For numerical stability purposes, for all graphite and silicon particles, we set the initial state of charge to 0.001 and 0.999, and voltage cutoff to 0.03V and 1V as end condition during lithiation and delithiation, respectively. The OCV of graphite, OCVs of silicon, and other inputs to Hybrid-MPET model of Si-Gr electrode are documented in Appendix A.

In Fig. 3 (a), we compare Hybrid-MPET model simulation and experimental measurement [24] of Li/Si-Gr cell performance. Our models are able to match the experimental cell voltages during both discharge (lithiation) and charge (delithiation). The effect of voltage hysteresis as seen in Fig. 2 can clearly be observed in the 0.05C lithiation and delithiation curves. Modelling hybrid porous electrodes introduces an additional layer of complexity through tracking the SOC of different active species. As seen in Fig. 3 (b), we show the simulated evolution of average SOC of silicon particles and graphite particles in the hybrid electrode at 0.05C operation from Hybrid-MPET model. These also match well with those predicted from other modeling and experimental studies of Si-Gr hybrid electrode at low current rates [30, 105]. While graphite shows consistent

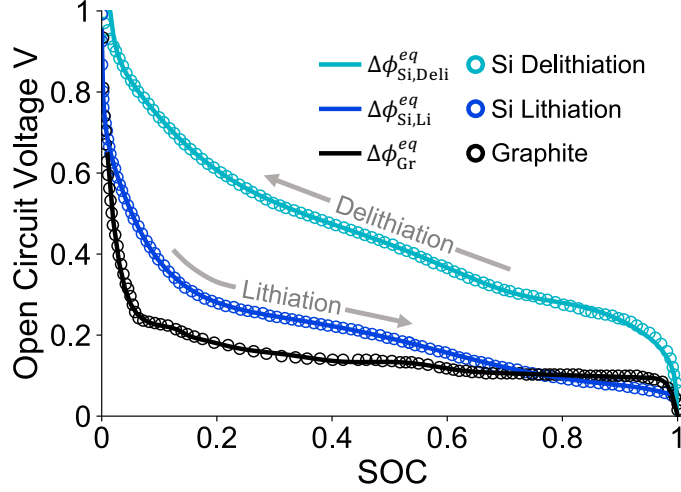


Figure 2: Open-circuit voltages as functions of state of charge for solid solution model of silicon and phase-field model of graphite. The experimentally measured OCVs of silicon[93] and graphite [104] are also shown, respectively.

lithiation and delithiation behavior, silicon clearly shows non-linearity and asymmetry behavior, which can be directly attributed to its OCV hysteresis. During lithiation, Li^+ intercalation reactions in silicon and graphite happen in parallel, and the rates are controlled by the reaction kinetics in Eq. 31. Note that in the same finite volume n , silicon and graphite particles share the same $\Delta\phi_n^s$ but experience different overpotentials because silicon and graphite have different OCVs. Thus, when reaction kinetics and transport are not limited at low current rates, silicon and graphite lithiation happen in parallel throughout the discharge process, yet the observed dominant active material is determined by thermodynamics, where the one with higher OCVs typically depletes earlier. The larger the OCV difference, the more distinct dominant active component is expected to be identified. As a result, compared to that of graphite, we expect silicon SOC to increase more rapidly at the beginning of lithiation as seen in Fig. 3(b) because silicon lithiation is initially driven by a larger overpotential. Silicon and graphite SOC will then proceed to increase individually as both particles support the total discharge current together. The cross intersection of silicon lithiation OCV and graphite OCV curves in Fig. 2 suggests that silicon lithiation reaction will then be driven by smaller overpotential than that of graphite. This change results in the observed fast reaction of the residual silicon at the end of discharge process, mostly only after the full lithiation of graphite.

The evolution of silicon and graphite SOC during delithiation is noticeably different from those during lithiation. Because $\Delta\phi_{\text{Gr}}^{\text{eq}}$ is much lower than $\Delta\phi_{\text{Si,Deli}}^{\text{eq}}$, a clearer order of deintercalation reactions is expected: most silicon only start to delithiate when the graphite has fully delithiated, as seen in the delithiation part of Fig. 3(b). Considering silicon has faster intercalation kinetics than graphite, we can design optimal cycling protocols for Si-Gr hybrid electrodes: for example, if we keep the half-cell setup, then during discharge

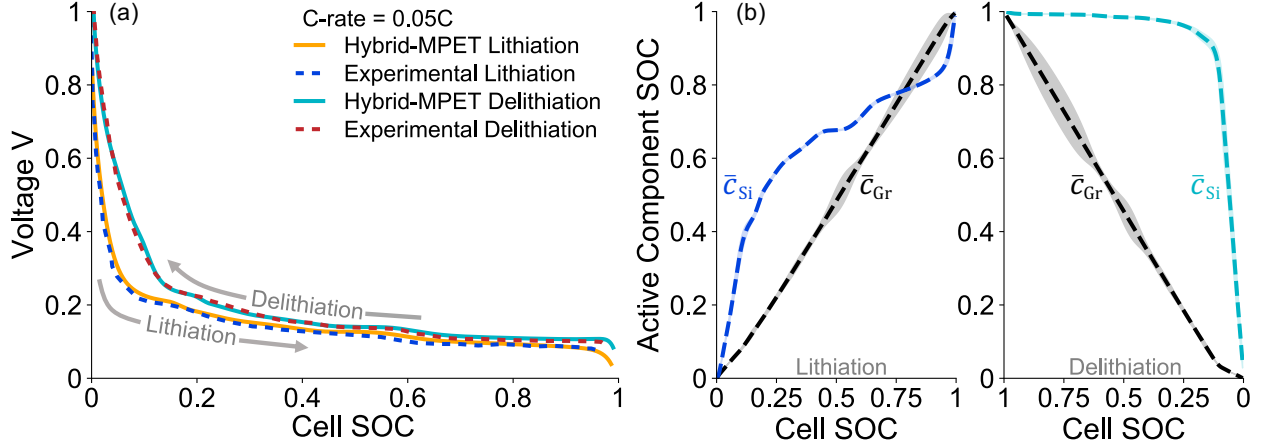


Figure 3: Hybrid-MPET simulation and experimental measurement [24] of silicon-graphite hybrid electrode performance during charge and discharge at 0.05C. (a) Cell voltage vs. Cell SOC (b) Active silicon and graphite utilization vs. Cell SOC from Hybrid-MPET simulation of lithiation and delithiation. The mean SOC of silicon and graphite particles are represented in dashed lines, and are accompanied by their respective 95% confidence intervals.

of Si-Gr hybrid cathode, we should start with high rate lithiation and then switch to low rate lithiation; during charging of Si-Gr hybrid cathode, we should start with low rate delithiation and then switch to high rate delithiation. Such step-wise operation protocols ensures that we maximize both silicon and graphite utilization in hybrid electrode and minimize charging and discharging duration by taking advantage of silicon's faster kinetics. Based on the analysis above, we expect monitoring the evolution of active component SOC's in a hybrid electrode to be a valuable tool in pinpointing the dominant reactant(s) and understanding their interactions under various operational protocols. It holds promise in providing insights on how each active component contributes to the macroscopic performance and assisting optimal operation protocol design for hybrid electrodes.

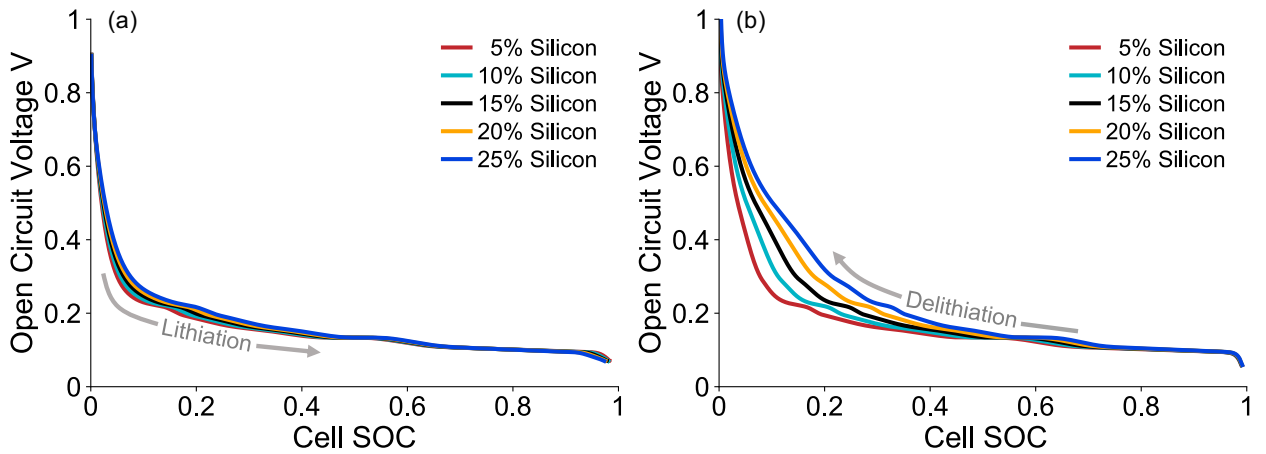


Figure 4: Hybrid-MPET prediction of the open circuit voltage of silicon-graphite hybrid electrode with varying silicon capacity fraction.

Through the introduction of volume correction terms in Eq. 12, Hybrid-MPET also has the versatility to predict performance of similar hybrid porous electrodes with any arbitrary targeted capacity fractions of silicon and graphite. We show the predicted OCVs of Si-Gr hybrid electrodes with different silicon capacity fraction in Fig. 4. The results were obtained by simulating lithiation and delithiation at $5 \times 10^{-6}\text{C}$ of the same Hybrid-MPET Si-Gr hybrid electrode model as above, but now the silicon capacity fractions vary between 0.05 to 0.25. The capacity fractions and subsequently, volume fractions of silicon were kept low intentionally such that volume changes of silicon particles still have minimal impact on performance. Still, different silicon capacity fraction leads to considerable amount of change in the OCV of Si-Gr hybrid electrodes. The predicted lithiation OCVs in Fig. 4(a) resembles a mix between the $\Delta\phi_{\text{Gr}}^{eq}$ and $\Delta\phi_{\text{Si,Li}}^{eq}$. For delithiation in Fig. 4(b), with increased silicon capacity fraction, the characteristic voltage plateaus of graphite occupy smaller range of cell SOC and the Si-Gr delithiation OCV gradually exhibits more traits of $\Delta\phi_{\text{Si,Deli}}^{eq}$ in Fig. 2. Since Hybrid-MPET models are able to accurately predict the impact of different capacity fraction of active components on the macroscopic voltage, we believe that Hybrid-MPET can support future development of hybrid electrodes with targeted voltage profiles by providing fast predictions of performance over wide a range of design parameters, including but not limited to selection of active materials and electrolytes, capacity fractions of active components, particle sizes, electrode porosity and thickness.

SVO and CF_x -SVO hybrid porous electrodes

High power density silver vanadium oxide $\text{Ag}_2\text{V}_4\text{O}_{11}$ (SVO) and high energy density carbon monofluoride (CF_x) have been traditionally used as cathode materials in lithium primary batteries powering pacemakers and ICDs, and the CF_x -SVO hybrid electrode has been developed to preserve the best properties of each [19–23]. The SVO that we focus on in this paper has C-centered monoclinic unit cell [44, 106], and is synthesized through solid state combination reaction of Ag_2O and V_2O_5 at high temperatures [44, 107]. During discharge, Li^+ insertion into SVO lattice is accompanied by two reversible parallel reactions: reduction of Ag^+ to metallic Ag and reduction of V^{5+} to V^{4+} [43, 44, 107, 108]. Due to the size differences between Ag^+ and Li^+ , increased Ag^+ displacement by Li^+ is accompanied by increased disorder and structural defects between vanadium oxide layers [43, 109–111]. The OCV of Li/SVO [44, 107, 112] has a voltage plateau at 3.24V covering the first $\frac{1}{3}$ cell capacity, strongly inferring coexistence of multiple stable phases throughout the Ag^+ displacement reaction. Another voltage plateau at 2.6V occupies the other $\frac{2}{3}$ cell capacity and corresponds to V^{5+} reduction, and most studies attribute it to Li^+ intercalation into an single-phase host structure with high degree of disorder [44, 107, 109, 113]. We recognize that further reduction of V^{4+} to V^{3+} has been observed in SVO when cell potential falls lower than 2.2V [107, 108, 114], but do not considered it because

the experimental data [112] we benchmark our models against do not reach such voltage ranges. As a result, in our models below, the capacity fraction of silver and vanadium are $\tilde{\rho}_{\text{Ag}} = \frac{1}{3}$ and $\tilde{\rho}_{\text{V}} = \frac{2}{3}$ in SVO. The composition $\text{Li}_2\text{V}_4\text{O}_{11}$ is complete silver depletion, and $\text{Li}_6\text{Ag}_2\text{V}_4\text{O}_{11}$ is full lithiation.

To show Hybrid-MPET’s capability of capturing transient behavior, we next validate a model of Li/SVO half-cell and capture its voltage overshoot phenomena observed during an accelerated data collection protocol. Its experimental data [112] is measured between near open-circuit low currents ($5\mu\text{A}$) to medium currents ($1000\mu\text{A}$) at 37°C , which resemble the rates needed by pacemakers and ICDs to perform basic background monitoring. Such low current rates are equivalent to $3.6 \times 10^{-6}\text{C}$ and $7.2 \times 10^{-4}\text{C}$, respectively, and would take many years to generate full voltage-capacity curves. To accelerate testing, multiple Li/SVO batteries were first discharged under $1000\mu\text{A}$ to different depths of discharge, then immediately switched to the desired lower current to create discontinuous discharge curves that were pieced together to form complete curves [112]. These unique accelerated data collection protocols have led to the observation of a voltage overshoot phenomenon: the voltage measured after Li/SVO switched from $1000\mu\text{A}$ to a near open-circuit low current is noticeably higher than cell voltage measured when Li/SVO is continuous galvanostatic discharged under that same low current. A subsequent relaxation process is required for the cell voltage to drop down. The existing single-particle model of Li/SVO [112] that treats SVO as a homogeneous solid solution material and has not been able to predict the voltage overshoot phenomena.

Note that similar voltage overshoots have been observed for LFP electrodes [115, 116] in response to intermittent galvanostatic discharge, and were attributed to the division of the LFP particle population into two distinct Li-rich and a Li-poor composition groups [53, 117–119] due to reaction heterogeneities [116] driven by the non-monotonic chemical potential of LFP. Since we only observe voltage overshoots in Li/SVO within its first $\frac{1}{3}$ depth of discharge, and since the existence of the 3.24V voltage plateau within first $\frac{1}{3}$ depth of discharge infers multiphase behavior, we hypothesize that introducing reaction heterogeneity during Ag^+ reduction could help capture the voltage overshoot phenomena in Li/SVO.

One option is to introduce reaction heterogeneity within SVO particles, which would lead to coexistence of two immiscible oxide phases with different concentrations of Ag and Li, one Ag-rich, Li-poor phase and another Ag-poor, Li-rich phase [44, 107, 113]. Metallic silver would also be at equilibrium [44, 107, 113] with two phases in SVO. The phase transition process in SVO during Ag^+ reduction likely resembles those during Li^+ insertion in Cu_yTiS_2 [120] and $\text{Cu}_3\text{Mo}_6\text{S}_8$ [121], where Cu-poor, Li-rich and Cu-rich, Li-poor materials were found at equilibrium with metallic Cu. However, compared to the clear characterization of two phases from X-ray diffraction (XRD) of LFP [122], characterization of stable phases in lithiated SVO is obscured by its disordered structure [43, 44, 109]: with increased lithiation, most observe loss of crystalline SVO phase, generation of metallic silver and a highly disordered lithiated SVO phase that retains of the basic vanadium

oxide layered structure with noticeable lattice parameter changes. There is currently very limited literature and phase mapping characterization that describes the exact mechanism of electrochemically driven phase transition during Ag^+ reduction, corresponding strain effects and moving phase boundaries in lithiated SVO particles. As a result, we do not have enough information to accurately model phase separation effects within SVO particles, whether it be through shrinking core models [75] or Cahn-Hillard phase field models [77, 78].

The other option is to introduce reaction heterogeneity across the SVO particle population by creating a many-particle model [123–125] in Hybrid-MPET. In this case, instead of focusing on phase separation within a single-particle, we would expect reaction heterogeneity across the SVO particles to divide particle population into two distinct groups, one at Ag-rich, Li-poor composition and the other at Ag-poor, Li-rich composition. At this scale, reaction heterogeneity is most likely caused by thermodynamics [52], kinetics [10], and particle size distribution [53]. Since most voltage overshoots were observed at near open-circuit low rate discharge of Li/SVO cells, it is unlikely that reaction heterogeneity is caused by kinetics or concentration polarization in electrolyte when reaction across all particles are already really slow. Another consequence of discharge at such low current rates is that reaction becomes much slower than Li^+ diffusion in SVO, and the SVO particles can be conveniently treated as homogeneous [112]. For industry grade SVO electrode, we expect no large size discrepancy exist across the SVO particle population and their particle sizes fall into a relatively narrow normal distribution.

We thus believe thermodynamics is the dominant driving force for creating reaction heterogeneity across SVO population at low current rates. We can create reaction heterogeneity across an ensemble of homogeneous SVO particles by introducing two energetically favorable compositions during Ag^+ reduction. To describe such thermodynamics, we formulate a double-well like homogeneous free energy as a function of only Ag state of charge c_{Ag} . The free energy has two local minima, which correspond to the stable Ag-rich, Li-poor composition $c_{\text{Ag},1}$ and Ag-poor, Li-rich composition $c_{\text{Ag},2}$. Similar to those in the many-particle models by Dreyer et al. [123, 124], the SVO particles in Hybrid-MPET model can also exchange Li^+ through interparticle pathways to lower their total energy as an ensemble. As a result, when the ensemble composition of SVO particles arrives between $c_{\text{Ag},1}$ and $c_{\text{Ag},2}$ and the electrode is relaxed, the SVO particles tend to lower their total free energy by separating into groups with composition $c_{\text{Ag},1}$ and $c_{\text{Ag},2}$. The second derivative of free energy also identifies the two metastable compositions [54, 67, 74, 126]: the Ag-rich, Li-poor one with composition c_{Ag,s_1} and a Ag-poor, Li-rich one with composition c_{Ag,s_2} , between which separation into two compositions groups becomes spontaneous. The lowered average free energy can be found by constructing a common tangent between the two local minima in the free energy, which corresponds to a voltage plateau with width $c_{\text{Ag},2} - c_{\text{Ag},1}$ in experimentally measured OCV. Therefore, while Ag^+ reduction reaction in single SVO particles has a non-monotonic homogeneous OCV $\Delta\phi_{\text{Ag}}^h$, it cannot be directly obtained from measuring macroscopic cell

voltage; the measured voltage plateau is instead the many-particle equilibrium potential $\Delta\bar{\phi}_{\text{Ag}}^{\text{eq}}$ [123, 124] that represents the emergent property of this divided SVO particle population. We can subsequently obtain a non-monotonic chemical potential and OCV for Ag^+ reduction reaction in individual SVO particles as seen in Fig. 5(a). The exact derivation [48, 67, 68] can be found in Appendix B.

Based on the analysis above, in our Hybrid-MPET model of Li/SVO, we define separate reaction kinetics and thermodynamics models for Ag^+ and V^{5+} reduction. For reaction kinetics, we use BV kinetics for both Ag^+ and V^{5+} reduction, and their exchange-current densities are fitted separately as functions of both electrolyte and solid concentrations. Compared to the conventional Li^+ intercalation reaction, it is commonly believed that the Ag^+ displacement reaction is kinetically slower [109]; such difference is in turn reflected in a relative smaller rate constant for Ag^+ reduction. For electrolyte transport, we use a concentrated Stefan Maxwell electrolyte model to represent a 1.1M LiAsF_6 in PC/DME in lithium-ion batteries. For thermodynamics, we use the aforementioned non-monotonic homogeneous OCV $\Delta\phi_{\text{Ag}}^h$ for Ag^+ reduction reaction. We fit a separate OCV $\Delta\phi_{\text{V}}^{\text{eq}}$ as a function of V^{5+} depth of discharge for V^{5+} reduction and treat the lithiated vanadium oxide as a solid solution material. The corresponding OCVs $\Delta\phi_{\text{Ag}}^h$, $\Delta\phi_{\text{V}}^{\text{eq}}$ can be seen in Fig. 5(a)(b). We discretize the hybrid porous electrode into 100 finite volumes, each containing 10 cylindrical homogeneous SVO particles. For numerical stability purposes, we set the initial depth of discharge of Ag^+ and V^{5+} to 0.01 in all SVO particles before discharge, and voltage cutoff to 2.2V as end condition. The free energy formulation, derivation of $\Delta\phi_{\text{Ag}}^h$, BV reaction kinetics, and other inputs to Hybrid-MPET model of SVO electrode are documented in Appendix B.

Note that for our Hybrid-MPET model of Li/SVO, we additionally make the following assumptions and simplifications: (a) we assume that subsequent nucleation of metallic silver atoms and growth of silver nanoparticles [45, 107] do not interfere with electrochemical reactions of Ag^+ and V^{5+} . Investigating the kinetics of nucleation and growth through using statistical models such as Kolmogorov–Johnson–Mehl–Avrami (KJMA) theory [127–129] is beyond the scope of the electrochemical P2D models, and we thus do not explicitly model the above processes in Hybrid-MPET. (b) we recognize that formation of highly conductive silver nanoparticles has been observed to considerably increase the electronic conductivity of SVO electrodes and film resistance at the Li metal anode can build up over time [43–45, 107], but expect such effects to be only limiting for high rate applications. (c) under the low discharge rates of Li/SVO battery below, we assume that other ohmic and transport resistances in solid and liquid phases are negligible.

In Fig. 6, we compare Hybrid-MPET model simulations and experimental measurements of Li/SVO battery discharge. We see that our Hybrid-MPET model of Li/SVO can not only accurately predict its continuous galvanostatic discharge at medium currents 640 μA , 1000 μA , but also captures the voltage overshoot phenomena prominent in the first $\frac{1}{3}$ cell capacity during accelerated data collection protocols: when the

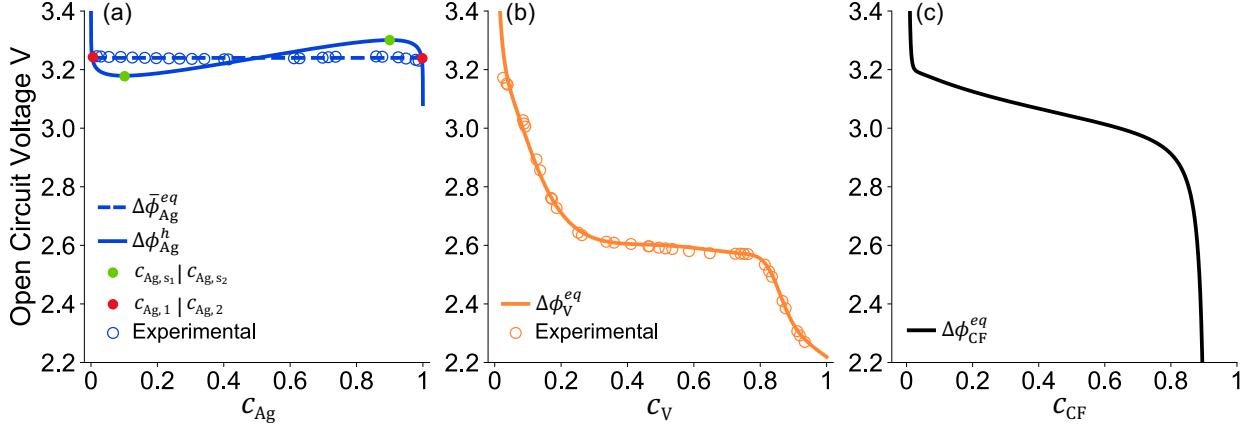


Figure 5: Open-circuit voltages as functions of state of charge for silver reduction, vanadium reduction, and carbon monofluoride reduction. The experimentally measured OCVs of SVO [44, 107, 112] is split by assuming that silver and vanadium reduction are dominant in the first $\frac{1}{3}$ and last $\frac{2}{3}$ capacity of SVO, respectively. (a) The non-monotonic $\Delta\phi_{Ag}^h$ is derived from a double-well like free energy function, which is formulated such that a common tangent construction between its two local energy minima has a composition width that matches the width of experimentally measured voltage plateau at 3.24V during Ag^+ reduction in the first $\frac{1}{3}$ capacity of SVO. the stable compositions $c_{Ag,1}$, $c_{Ag,2}$ and metastable compositions $c_{Ag,s1}$, $c_{Ag,s2}$ are also shown. (b) $\Delta\phi_V^{eq}$ is fitted as a function of vanadium utilization from the data in last $\frac{2}{3}$ capacity of SVO. (c) $\Delta\phi_{CF}^{eq}$ is extracted from experimental data [112] by assuming Tafel kinetics.

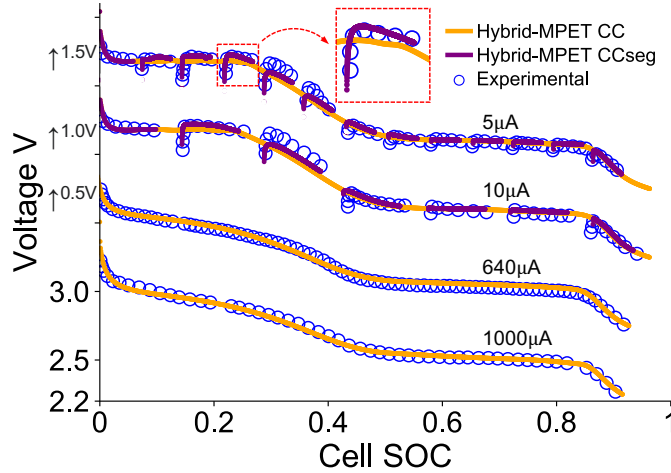


Figure 6: Hybrid-MPET model simulations and experimental measurements [112] of Li/SVO under both continuous galvanostatic discharge at 5 μA , 10 μA , 640 μA , 1000 μA and accelerated data collection protocols where capacity release at 1000 μA is followed by instantaneous switch to discharging at near open-circuit low currents 5 μA or 10 μA [112]. 5 μA , 10 μA , 640 μA , 1000 μA for this Li/SVO cell are equivalent to $3.6 \times 10^{-6} C$, $7.2 \times 10^{-6} C$, $4.6 \times 10^{-4} C$ and $7.2 \times 10^{-4} C$. For clarity purposes, we vertically shift up the simulations and experimental data corresponding to 5 μA , 10 μA , and 640 μA by 1.5V, 1V, and 0.5V, respectively.

switch from 1000 μA to 5 μA or 10 μA happens, our model predicts that the cell voltage raises rapidly to a value higher than predicted the cell voltage at the same cell SOC when Li/SVO is continuous galvanostatic discharged under 5 μA or 10 μA . To explore the root cause of the voltage overshoot phenomena, we show

the predicted evolution of silver utilization across the SVO particles when Li/SVO is discharged under near open-circuit low current rate $5\mu\text{A}$ and medium current rate $1000\mu\text{A}$ in Fig. 7. It is clear that under those two currents, the Hybrid-MPET model predicts that population dynamics of the SVO particles are very different besides at the beginning of discharge and near depletion of silver in most SVO particles.

On the one hand, a bimodal population is observed under $5\mu\text{A}$ discharge in Fig. 7 (a), which shows the separation of SVO particle population into two groups towards Ag-rich, Li-poor and Ag-poor, Li-rich compositions. Such separation is driven by a strong reaction heterogeneity, which we introduced through using a non-monotonic $\Delta\phi_{\text{Ag}}^h$ derived from a double-well like free energy. Under $5\mu\text{A}$ discharge, the current is near open-circuit, and the evolution of depth of discharge in SVO particles will follow the thermodynamically favored path. As a result, during initial stages of discharge, with increased lithiation, the compositions of SVO particles move homogeneously towards the Ag-rich, Li-poor compositions $c_{\text{Ag},1}$ and subsequently c_{Ag,s_1} . However, continuous discharge of the electrode means that Ag^+ needs to be reduced for Li^+ to be inserted, and composition changes have to happen somewhere between the SVO particles. The most thermodynamically favored pathway is for Ag^+ reduction and Li^+ insertion to take place only in a few particles in the porous electrode. These few particles undergo phase transition, where their compositions gradually move towards the Ag-poor, Li-rich metastable composition c_{Ag,s_2} while rest of the particles remain mostly inactive at Ag-rich, Li-poor compositions. As discharge proceeds, once the compositions of the few particles reach c_{Ag,s_2} , a few previously inactive particles will initiate their transition from c_{Ag,s_1} to c_{Ag,s_2} . As seen from Fig. 7 (a), the fraction of active particles remains small throughout this "mosaic" particle-by-particle reaction process, which has been predicted and observed for other electrode materials [50, 52, 53, 55, 56, 117, 118, 123]. In Fig. 7 (c), by comparing the silver utilization across 10 homogeneous SVO particles in a representative finite volume from Hybrid-MPET model at two different cell SOC, the particle-by-particle reaction is clearly observed when discharging under $5\mu\text{A}$. Once all particles reach composition c_{Ag,s_2} , they then eventually reach full silver depletion as a homogeneous ensemble and only then do we start to see significant changes in vanadium depth of discharge in SVO particles.

On the other one hand, an unimodal population is observed under $1000\mu\text{A}$ discharge in Fig. 7 (b). Reactions take place concurrently across SVO particle population and leads to homogeneous utilization of silver in the electrode. While separation of population into two composition groups is thermodynamically favored, larger current rates demand faster kinetics, and most if not all SVO particles need to concurrently [52] support the larger current. Examining both Fig. 7 (b) and (d), we clearly see that the unimodal population is preserved throughout the discharge process until silver depletion, and the separation of particle population into two composition groups is suppressed by the relatively faster kinetics at $1000\mu\text{A}$. While $1000\mu\text{A}$ is $200\times$ increase in current compared to $5\mu\text{A}$, $1000\mu\text{A}$ (equivalent to $7.2\times 10^{-4}\text{C}$) is still low enough such that Ag^+

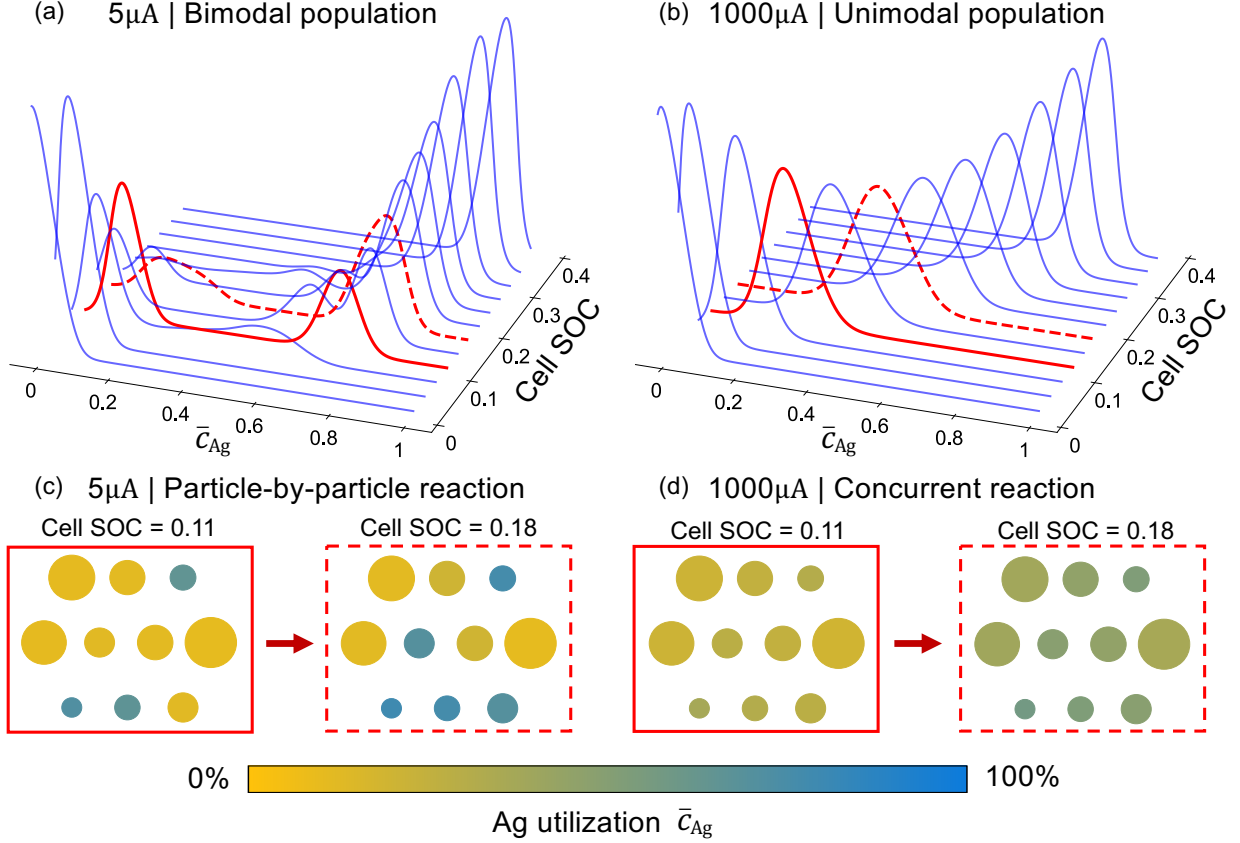


Figure 7: (a)(b) Evolution of probability density estimate of silver utilization across the SVO particle population when Li/SVO cell is discharged under constant current 5 μ A and 1000 μ A. Cell SOC acts as a proxy for time, and thus we can infer population dynamics by examining the gaussian kernel density estimate at different cell SOC. The firm and dashed red curve represent silver utilization distribution across the particle ensemble at SOC = 0.11 and 0.18, respectively. (c)(d) The development of silver utilization across 10 homogeneous SVO particles in a representative finite volume from Hybrid-MPET model when discharge occurs under 5 μ A and 1000 μ A, respectively. For visualization clarity, we show the cylindrical SVO particles along the axial direction.

reduction still remains mostly dominant. The animated short videos of Fig. 7 (a) and (b) can be found in the Supplementary Material.

Based on the analysis above, the root-cause of the voltage overshoot phenomena seen in the first $\frac{1}{3}$ capacity of Li/SVO becomes quite clear. The comparison will be between the following two cases at the same cell SOC: (1) immediate switch to low current 5 μ A after fast capacity release under medium current 1000 μ A in an accelerated data collection protocol (2) continuous discharge under 5 μ A. Its 1000 μ A discharge history means that case (1) has a significantly larger fraction of active particles due to previous concurrent reaction driven by medium current 1000 μ A. Case (1) has more homogeneous reaction across the porous electrode while the current in case (2) is only supported by a small fraction of the porous electrode, resulting in fundamentally different battery resistant states from a more macroscale and empirical perspective. As a

result, when the demand of a 5 μ A current is the same, the overpotentials experienced by a large number of SVO particles in case (1) is smaller than those experienced by the smaller number of SVO particles in case (2), resulting in an observed voltage overshoot. For case (1), as the current is held at near open-circuit low rates for longer, thermodynamics soon becomes dominant over kinetics, and the previously homogeneous particle population start to separate towards two groups at Ag-rich, Li-poor and Ag-poor, Li-rich compositions despite continuous slow discharge. The previously concurrent reaction across all particles gradually transitions to the particle-by-particle like reaction as more particles reach their energetically favorable compositions, and thus the fraction of active particles gradually decreases. Such transition is predicted to be slow, and corresponds to the "relaxation" process where the overshooted voltage in case (1) to slowly returns to the cell voltage values of case (2). The animated short video on evolution of silver utilization across SVO particle population during this transition can be found in the Supplementary Material.

While the existing single-particle model of Li/SVO [112] could predict battery performance under constant current discharge, it was unable to capture the voltage overshoot phenomena because it extrapolated battery performance directly from single-particle dynamics by assuming uniform current across its electrode. In batteries, current rate dependent reaction heterogeneities [49, 52] are commonly observed and often need to be introduced into battery models at particle or electrode scale to capture the correct macroscopic experimental phenomena. Because SVO was assumed to not be diffusion limited at such low current rates, only inter-particle scale reaction heterogeneities were observed and intra-particle scale concentration gradients were not considered in Hybrid-MPET model above. However, such assumptions may not hold at much high current rates. By leveraging MPET's ability to predict reaction heterogeneities at multiple scales, Hybrid-MPET has the potential to accurately predict the performance of hybrid porous electrodes over a wider range of current rates.

We finally test our Hybrid-MPET model of Li/CF_x-SVO half-cells. CF_x is synthesized through direct fluorination of carbon [130, 131]. In these Li/CF_x-SVO half-cells[112], it is estimated that $x \approx 1$ in CF_x, and we assume CF_x particles consist of a single CF phase. Its electrochemical reduction reaction to LiF and C has been experimentally observed to be irreversible [130] and we thus adopt Tafel kinetics for electrochemical reduction of CF_x [112, 132, 133]. For electrolyte transport, we use a concentrated Stefan Maxwell electrolyte model to represent a 1.1M LiBF₆ in GBL/DME in lithium-ion batteries. The rate constants in BV reaction kinetics of both Ag⁺ and V⁵⁺ reduction are thus refit due to the use of a different electrolyte. For thermodynamics, the OCV of CF_x $\Delta\phi_{CF}^{eq}$ as seen in Fig. 5(c) is extracted from experimental data [112] by assuming Tafel kinetics, which is then fitted directly as a function of CF_x utilization and resembles the CF_x cathode's measured OCV between 3.2V and 3.4V [130, 133] in most non-aqueous liquid electrolytes. We discretize the hybrid porous electrode into 100 finite volumes, each containing 10 cylindrical SVO and 2 spherical CF_x particles. For most

geometric and physical properties of the cell, electrode, and particles, we reference the values from Gomadam et al [112]. For numerical stability purposes, we set the initial depth of discharge of Ag^+ , V^{5+} , and CF to 0.01 in all SVO and CF_x particles before discharge, and voltage cutoff to 2.2V as end condition. The $\Delta\phi_{\text{CF}}^{\text{eq}}$, Tafel kinetics of CF_x , and other inputs to Hybrid-MPET model of Li/ CF_x -SVO batteries are documented in Appendix C. We keep our previous assumptions and simplifications in Hybrid-MPET model of Li/SVO for Hybrid-MPET models Li/ CF_x -SVO batteries, and introduce an additional one: we acknowledge that as $x \approx 1$ in CF_x , C-F bonding becomes increasingly covalent, leading to poor conductivity [130, 132] of CF_x cathode. It is assumed that sufficient conductivity aid is added to the CF_x -SVO hybrid porous electrode such that the ohmic resistance from solid remains negligible at the relatively low current rates below, and the higher fraction of inactive material is reflected in lower active material volume loadings P_L of HB1-HB4 as seen in Appendix C.

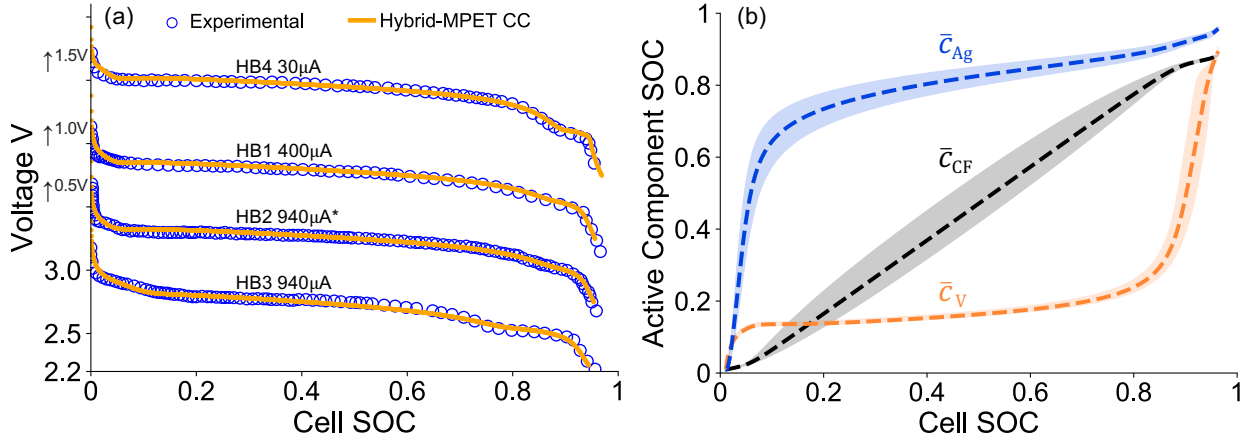


Figure 8: Hybrid-MPET prediction and experimental measurements [112] of the galvanostatic discharge of hybrid cathode Li/ CF_x -SVO batteries with varying CF_x and SVO capacity fractions. (a) Cell voltage vs. Cell SOC of four Li/ CF_x -SVO batteries with similar sizes under different current rates. HB1, HB2, HB4 have SVO capacity fraction 0.128, and HB3 has SVO capacity fraction 0.333. The listed discharge currents for HB1 - HB4 are equivalent to $1.9 \times 10^{-5}\text{C}$, $5.2 \times 10^{-4}\text{C}$, $7.9 \times 10^{-4}\text{C}$, and $9.0 \times 10^{-4}\text{C}$. For clarity purposes, we vertically shift up the simulations and experimental data corresponding to HB4 30 μA, HB1 400 μA, and HB2 940 μA by 1.5V, 1V, and 0.5V, respectively. (b) Active silver, vanadium, and carbon monofluoride utilization vs. Cell SOC from Hybrid-MPET simulation of HB2 Li/ CF_x -SVO battery under 940 μA galvanostatic discharge. The average utilization of active silver and vanadium, and carbon monofluoride are represented in dashed lines, and are accompanied by their respective 95% confidence intervals.

In Fig. 8 (a), we compare Hybrid-MPET model simulations and experimental measurements of Li/ CF_x -SVO performance. For the 4 CF_x -SVO hybrid cathodes with different geometric sizes and CF_x and SVO capacity fractions, our model is able to accurately predict cell voltages during discharge under low to medium current rates when compared to experimental data. Compared to HB2, HB3 has considerably larger SVO capacity fraction, and such difference is accurately reflected by the Hybrid-MPET model predictions: larger SVO capacity fraction correspond to larger vanadium capacity fraction, which yields a longer characteristic

voltage plateau at 2.6V for HB3. To examine the actively reacting component at different cell SOC, in Fig. 8 (b), we show the Hybrid-MPET model predicted evolution of average depth of discharge of silver, vanadium and carbon monofluoride in the hybrid porous cathode of HB2 when discharged under 940 μA . Again, we see that when reaction kinetics and transport are not limited at such low current rates, the three reduction reactions take place in parallel and the observed dominant active component is determined by thermodynamics: silver, vanadium, and carbon monofluoride share the same electrode potential in the same finite volume, are at equilibrium but experience different overpotentials due to each having its own OCV that is dependent on its own depth of discharge. Based on the height differences of OCVs as in Fig. 5, the expected order of depletion is silver, carbon monofluoride, and vanadium, which is indeed observed in Fig. 8 (b). During initial stages of discharge, Ag^+ reduction is dominant while V^{5+} reduction takes place in parallel to maintain equilibrium potential with silver in SVO. This prediction matches observations from many experimental studies [43–45, 109, 112, 134], which have argued that V^{5+} reduction could precede Ag^+ reduction and support that they are more parallel rather than sequential. Meanwhile, no significant reaction heterogeneity is observed across SVO particles, and the separation of SVO particle population into two composition groups is again suppressed by the relatively faster kinetics at 940 μA . The loss of capacity brings the cell voltage down to values where CF_x becomes the primary active component to support the discharge current through its reduction, during which most residual silver is depleted while vanadium utilization stays nearly constant. When CF_x reaches near depletion, V^{5+} reduction becomes dominant until the end of discharge. The Hybrid-MPET model prediction of silver, vanadium and carbon monofluoride utilization as seen in Fig. 8 (b) match well with those from other modeling studies of Li/ CF_x -SVO batteries [112]. Note that the observed depletion order is expected to be true only under low current rates where thermodynamics are dominant over kinetics and transport limitations are neglected; it is highly likely that such depletion order is no longer held at higher current rates. For example, it has been experimentally observed [22, 23] that at high current pulses, SVO provides most of the power due to its higher rate capability while during post-pulse relaxation at low currents, CF_x discharges itself to recharge SVO until both are at equilibrium. Such complicated interactions between different active materials offers great opportunities for future modeling studies using Hybrid-MPET.

Conclusion

Despite the increasing research and application interest in hybrid electrode batteries, there is a lack of open-source battery simulation software that are suited for them. To address this issue, we present Hybrid-MPET, a mathematical modeling framework and open-source battery simulation software package. Hybrid-MPET is

implemented based on the MPET framework [48], and its key modifications have been described in detail. Through sample case studies of Si-Gr, SVO, and CF_x -SVO hybrid porous electrodes, we have illustrated the novel features of Hybrid-MPET models, including but not limited to its ability to: (1) account for intra-particle scale and inter-particle scale parallel reactions (2) accommodate both phase separating and solid solution type active electrode materials in the same simulation (3) allow free combination of active materials of interest at any capacity fraction in the hybrid electrode. (4) predict the evolution of state of charge for each active material through charge and discharge processes (5) capture the impact of particle scale reaction heterogeneity on macroscopic battery performance.

Since Hybrid-MPET is open-sourced and inherits the modular design from MPET, we encourage its reuse, modification, and optimization. Modelling hybrid porous electrodes is exciting but also challenging because they offer an entire new dimension of complexity, where the state of charge needs to be tracked separately for different active materials. Despite reactions from each active material being parallel, the clear sequential depletion orders observed in the sample simulations are mostly true at low current rates, where thermodynamics are dominant. However, at higher current rates, the limitations from kinetics and transport is expected to have greater impact.

A natural extension of this work would be towards using Hybrid-MPET models to simulate performance of hybrid electrode at higher current rates; we also expect high currents to drive the its active materials to far-from-equilibrium states, and have great interest in studying capacity exchange between the different active materials during post-pulse relaxation. As hybrid electrodes open a vast new design space and require more comprehensive testing protocols, we believe Hybrid-MPET has great potential to complement experimental research and accelerate the future development of hybrid electrodes with targeted voltage profiles by providing fast and accurate predictions of battery performance.

Another important extension would be to develop degradation models for Hybrid MPET. The literature on battery degradation has focused almost exclusively on single-component electrodes, notably graphite, using coarse-grained models of the key capacity-fade mechanisms, such as solid-electrolyte-interphase (SEI) growth [135] and electrochemomechanical fatigue [136]. Both of these phenomena are much stronger in silicon than in graphite, so the blending of silicon in graphite to achieve higher energy density must be balanced against the acceleration of capacity fade [137, 138]. Hybrid cathodes involving different transition metal oxides will also undergo oxidative surface degradation at different rates, depending on their stoichiometries [139]. Some critical degradation reactions, such as lithium metal plating in graphite anodes (also affecting battery safety), are also known to be strongly coupled with phase separation dynamics [16, 17, 90, 140]. The coupling of different degradation mechanisms and rates for the various components of hybrid electrodes will have a nontrivial dependence on microstructure and composition, which could be unraveled more easily with the

help of Hybrid-MPET simulations that also account for heterogeneity arising from phase transformations.

Code availability

The code for Hybrid-MPET battery simulation software is available in the following GitHub repository [141]:
<https://github.com/HarryQL/Hybrid-MPET>

Acknowledgements

This work is supported by Medtronic Public Limited Company.

Appendix A

We postulate a free energy functional describing the physics of the graphite particle, and separate it into homogeneous and non-homogenous free energy. Following van der Waals [142] and Cahn and Hilliard [77], we use a simple gradient penalty term to describe the non-homogeneous free energy, and obtain [17, 48] the following the diffusional chemical potential μ_{Gr} of Li^+ in inserted into graphite is defined as,

$$\mu_{\text{Gr}}(c_{\text{Gr}}) = \frac{\delta G}{\delta c_{\text{Gr}}} = \frac{\partial g}{\partial c_{\text{Gr}}} - \nabla \cdot \frac{\partial g}{\partial \nabla c_{\text{Gr}}} = -0.02 + \mu_1 + \mu_2 + \mu_3 + \mu_4 + \mu_5 - \frac{\kappa}{\rho_{\text{Gr}}} \nabla^2 c_{\text{Gr}} \quad (18)$$

$$\begin{aligned} \mu_1 = k_{\text{B}}T \left[\left(-30 \exp \left(-\frac{c_{\text{Gr}}}{0.025} \right) - 2(1 - c_{\text{Gr}}) \right) S_D(c_{\text{Gr}}, 0.38, 0.05) + 0.7 \left(\tanh \left(\frac{c_{\text{Gr}} - 0.37}{0.075} \right) - 1 \right) \right. \\ \left. + 0.8 \left(\tanh \left(\frac{c_{\text{Gr}} - 0.2}{0.06} \right) - 1 \right) + 0.38 \left(\tanh \left(\frac{c_{\text{Gr}} - 0.14}{0.015} \right) - 1 \right) \right] S_D(c_{\text{Gr}}, 0.42, 0.05) \end{aligned} \quad (19)$$

$$\mu_2 = -k_{\text{B}}T \frac{0.05}{c_{\text{Gr}}^{0.55}} \quad (20)$$

$$\mu_3 = 10k_{\text{B}}T S_U(c_{\text{Gr}}, 1, 0.015) \quad (21)$$

$$\mu_4 = 1.8\tilde{\Omega}_a k_{\text{B}}T (0.17 - c_{\text{Gr}}^{0.98}) S_D(c_{\text{Gr}}, 0.55, 0.045) S_U(c_{\text{Gr}}, 0.38, 0.05) \quad (22)$$

$$\mu_5 = k_B T \left[0.4\tilde{\Omega}_a(0.74 - c_{Gr}) + 0.55\tilde{\Omega}_b - 2(1 - c_{Gr}) \right] S_U(c_{Gr}, 0.6, 0.04) \quad (23)$$

where $\tilde{\Omega}_a = 0.81169$, $\tilde{\Omega}_b = 2.2214$, $k_B = 1.38 \times 10^{-23} \frac{J}{K}$, and $T = 298.15K$. Step-up and step-down functions are defined as [17],

$$S_D(c_{Gr}, c_x, \delta) = 0.5 \left(-\tanh \left(\frac{c_{Gr} - c_x}{\delta} \right) + 1 \right) \quad (24)$$

$$S_U(c_{Gr}, c_x, \delta) = 0.5 \left(\tanh \left(\frac{c_{Gr} - c_x}{\delta} \right) + 1 \right) \quad (25)$$

Subsequently, the OCV for graphite is,

$$\Delta\phi_{Gr}^{eq}(c_{Gr}) = 0.12 - \frac{\mu_{Gr}(c_{Gr})}{e} \quad (26)$$

where $e = 1.602 \times 10^{-19}C$, and 0.12 volts is a fitted reference potential $\Delta\phi_{Gr}^o(c_{Gr})$ [48, 67].

The OCVs for silicon lithiation and delithiation are fitted separately as,

$$\begin{aligned} \Delta\phi_{Si,Li}^{eq} = & 0.284 - 0.084 \ln \left(\frac{c_{Si}}{1 - c_{Si}} \right) \\ & + \frac{0.022c_{Si} - 0.711c_{Si}^2 + 2.673c_{Si}^3 - 3.762c_{Si}^4 + 0.246c_{Si}^5 + 3.588c_{Si}^6 - 2.050c_{Si}^7}{0.007 + 0.131c_{Si} + 1.158c_{Si}^2 - 1.120c_{Si}^3 - 0.290c_{Si}^4 + 0.790c_{Si}^5 - 0.657c_{Si}^6} \end{aligned} \quad (27)$$

$$\begin{aligned} \Delta\phi_{Si,Deli}^{eq} = & 0.948 - 0.006 \ln \left(\frac{c_{Si}}{1 - c_{Si}} \right) \\ & + \frac{-1.093c_{Si} + 2.886c_{Si}^2 - 1.670c_{Si}^3 - 2.133c_{Si}^4 + 0.529c_{Si}^5 + 1.895c_{Si}^6 - 0.509c_{Si}^7}{0.362 + 0.230c_{Si} - 2.027c_{Si}^2 + 1.568c_{Si}^3 + 1.181c_{Si}^4 + 1.046c_{Si}^5 - 2.249c_{Si}^6} \end{aligned} \quad (28)$$

The reaction kinetics of graphite and silicon are,

$$i_{Gr} = j_{Gr}e = k_{Gr}(c^l)^{0.5}c_{Gr}^{0.5}(1 - c_{Gr})^{0.5} \left[\exp \left(-\frac{\alpha_{Gr}e\eta_{Gr}^{eff}}{k_B T} \right) - \exp \left(\frac{(1 - \alpha_{Gr})e\eta_{Gr}^{eff}}{k_B T} \right) \right] \quad (29)$$

$$i_{Si} = j_{Si}e = k_{Si}(c^l)^{0.5}c_{Si}^{0.5}(1 - c_{Si})^{0.5} \left[\exp \left(-\frac{\alpha_{Si}e\eta_{Si}^{eff}}{k_B T} \right) - \exp \left(\frac{(1 - \alpha_{Si})e\eta_{Si}^{eff}}{k_B T} \right) \right] \quad (30)$$

The separator used has thickness 12 μm , porosity 0.47 [24], and tortuosity ϵ^{-1} , and is discretized into 2 finite

volumes. The other key parameters used in Hybrid-MPET model of Li/Si-Gr can be seen in Table 1,

Table 1: Geometric and materials properties used in simulating silicon-graphite hybrid porous electrode

Parameter	Description	Unit	Si-Gr Hybrid Porous Electrode	
L	thickness	μm	85.2 [24]	
ϵ	porosity	-	0.25 [24]	
P_L	active solid volume fraction	-	0.87	
τ	tortuosity	-	$\epsilon^{-0.2}$	
\tilde{Q}_{Si}	capacity fraction of silicon	-	0.086	
\tilde{Q}_{Gr}	capacity fraction of graphite	-	0.914	
Parameter	Description	Unit	Graphite	Silicon
R	particle radius	μm	$\mathcal{N}(5.86, 1.2)$ [24]	$\mathcal{N}(1.52, 0.8)$ [24]
ρ	volumetric site density	mol m^{-3}	29700 [104]	277990 [143]
D	diffusion coefficient	m^2s^{-1}	5.5×10^{-14} [30]	-
α	symmetry coefficient	-	0.5	0.5
k	rate constant	A m^{-2}	1	40

Adopting Eq. 13 and 16 for Si-Gr, we have the following inter-particle scale equations are,

$$\bar{c}_n^{corr} = \frac{\sum_{p_{Si}=1}^{P_{Si}} \rho_{Si} V_{n,p_{Si}} f_{n,Si} \bar{c}_{n,p_{Si}} + \sum_{p_{Gr}=1}^{P_{Gr}} \rho_{Gr} V_{n,p_{Gr}} f_{n,Gr} \bar{c}_{n,p_{Gr}}}{\sum_{p_{Si}=1}^{P_{Si}} \rho_{Si} V_{n,p_{Si}} f_{n,Si} + \sum_{p_{Gr}=1}^{P_{Gr}} \rho_{Gr} V_{n,p_{Gr}} f_{n,Gr}} \quad (31)$$

$$R_n^{V,corr} = -(1 - \epsilon) P_L \left(\sum_{p_{Si}=1}^{P_{Si}} \tilde{V}_{n,p_{Si}} \frac{\partial \bar{c}_{n,p_{Si}}}{\partial t} + \sum_{p_{Gr}=1}^{P_{Gr}} \tilde{V}_{n,p_{Gr}} \frac{\partial \bar{c}_{n,p_{Gr}}}{\partial t} \right) \quad (32)$$

where the corrected volume fractions are

$$\tilde{V}_{n,p_{Si}} = \frac{V_{n,p_{Si}} f_{n,Si}}{\sum_{p_{Si}=1}^{P_{Si}} V_{n,p_{Si}} f_{n,Si} + \sum_{p_{Gr}=1}^{P_{Gr}} V_{n,p_{Gr}} f_{n,Gr}} \quad (33)$$

$$\tilde{V}_{n,p_{Gr}} = \frac{V_{n,p_{Gr}} f_{n,Gr}}{\sum_{p_{Si}=1}^{P_{Si}} V_{n,p_{Si}} f_{n,Si} + \sum_{p_{Gr}=1}^{P_{Gr}} V_{n,p_{Gr}} f_{n,Gr}} \quad (34)$$

Appendix B

To describe the thermodynamics of Ag^+ reduction, we postulate a double-well like free energy functional without non-homogeneous terms (e.g. gradient penalty or coherent stress),

$$g^h = k_B T [c_{Ag} \ln(c_{Ag}) + (1 - c_{Ag}) \ln(1 - c_{Ag})] + \tilde{\Omega}_a k_B T c_{Ag} (1 - c_{Ag}) \quad (35)$$

where $T = 310.15K$ and $\tilde{\Omega}_a = 5.6$. The first-derivative of g^h yields two stable phase compositions at $c_{Ag,1} = 0.003845$ and $c_{Ag,2} = 0.996155$. The diffusional chemical potential μ_{Ag}^h of Li^+ in inserted into SVO due to Ag^+ reduction is,

$$\mu_{Ag}^h(c_{Ag}) = \frac{\partial g}{\partial c_{Ag}} = k_B T \ln\left(\frac{c_{Ag}}{1 - c_{Ag}}\right) + \tilde{\Omega}_a k_B T (1 - 2c_{Ag}) \quad (36)$$

The second-derivative g^h or the first-derivative of μ_{Ag}^h yields two metastable phase compositions at $c_{Ag,s1} = 0.09911$ and $c_{Ag,s2} = 0.90089$. The homogeneous OCV $\Delta\phi_{Ag}^h$ used in the simulation is thus,

$$\Delta\phi_{Ag}^h(c_{Ag}) = 3.24 - \frac{\mu_{Ag}^h(c_{Ag})}{e} \quad (37)$$

The thermodynamics of V^{5+} reduction is described by using a separate OCV function $\Delta\phi_V^{eq}$, fitted directly as a function of its depth of discharge c_V [112],

$$\Delta\phi_V^{eq}(c_V) = 0.823 + \exp(-80c_V) + \frac{3.177 + 92.839c_V^2 + 49.148c_V^4 - 658.841c_V^6 + 589.917c_V^8}{1 + 39.404c_V^2 - 6.299c_V^4 - 171.554c_V^6 + 106.016c_V^8 + 65.794c_V^{10}} \quad (38)$$

The reaction kinetics of Ag^+ and V^{5+} reduction used are,

$$i_{Ag} = j_{Ag}e = k_{Ag}(c^l)^{0.5}c_{Ag}^{0.1}(1 - c_{Ag})^{5.5} \left[\exp\left(-\frac{\alpha_{Ag}e\eta_{Ag}^{eff}}{k_B T}\right) - \exp\left(\frac{(1 - \alpha_{Ag})e\eta_{Ag}^{eff}}{k_B T}\right) \right] \quad (39)$$

$$i_V = j_Ve = k_V(c^l)^{0.5}c_V^{0.5}(1 - c_V)^{0.5} \left[\exp\left(-\frac{\alpha_Ve\eta_V^{eff}}{k_B T}\right) - \exp\left(\frac{(1 - \alpha_V)e\eta_V^{eff}}{k_B T}\right) \right] \quad (40)$$

The separator used has thickness $50\mu m$, porosity 0.4, and tortuosity $\epsilon^{-0.6}$, and is discretized into 10 finite volumes. The other key parameters used in Hybrid-MPET model of Li/SVO can be seen in Table 2 and many reference Gomadam et al. [112],

Adopting Eq. 4, 6, and 9 for SVO, and considering $\rho_{Ag} = \frac{1}{3}\rho_{SVO}$, $\rho_V = \frac{2}{3}\rho_{SVO}$, we have the following intra-particle scale equations,

$$\bar{c}_{n,p} = \frac{1}{3}\bar{c}_{n,p,Ag} + \frac{2}{3}\bar{c}_{n,p,V} \quad (41)$$

$$R_n^V = -(1 - \epsilon)P_L \sum_{p=1}^P \tilde{V}_{n,p} \left(\frac{1}{3} \frac{\partial \bar{c}_{n,p,Ag}}{\partial t} + \frac{2}{3} \frac{\partial \bar{c}_{n,p,V}}{\partial t} \right) \quad (42)$$

Table 2: Geometric and materials properties used in simulating SVO hybrid porous electrode

Parameter	Description	Unit	SVO Hybrid Porous Electrode	
L	thickness	mm	2.6	
ϵ	porosity	-	0.20	
P_L	active solid volume fraction	-	0.95	
τ	tortuosity	-	$\epsilon^{-0.6}$	
Parameter	Description	Unit	Ag	V
R	particle radius	μm	$\mathcal{N}(1, 0.3)$	
h	particle length	μm	20	
ρ	volumetric site density	mol m^{-3}	16107	32215
α	symmetry coefficient	-	0.5	0.5
k	rate constant	A m^{-2}	2×10^{-4}	7×10^{-1}

where again $\tilde{V}_{n,p} = \frac{V_{n,p}}{\sum_{p=1}^P V_{n,p}}$ is volume fraction of particle p in finite volume n .

Appendix C

$\Delta\phi_{\text{CF}}^{eq}$ is extracted from experimental data by assuming Tafel kinetics, and fitted directly as a function of its depth of discharge c_{CF} ,

$$\begin{aligned} \Delta\phi_{\text{CF}}^{eq}(c_{\text{CF}}) = & -0.077 - 0.047 \ln \left(c_{\text{CF}}(1 - c_{\text{CF}})^{\frac{1}{3}} \right) \\ & + \frac{5.566 - 1476.243c_{\text{CF}} + 240158.880c_{\text{CF}}^2 - 116028.195c_{\text{CF}}^3 - 166268.131c_{\text{CF}}^4 + 4436.904c_{\text{CF}}^5}{1 - 404.085c_{\text{CF}} + 75655.382c_{\text{CF}}^2 - 32080.426c_{\text{CF}}^3 - 55461.302c_{\text{CF}}^4} \end{aligned} \quad (43)$$

The reaction kinetics of carbon monofluoride is,

$$i_{\text{CF}} = j_{\text{CF}} e = k_{\text{CF}} c_{\text{CF}} (1 - c_{\text{CF}}) \left[\exp \left(-\frac{\alpha_{\text{CF}} e \eta_{\text{CF}}^{\text{eff}}}{k_{\text{B}} T} \right) \right] \quad (44)$$

The separator used has thickness 50 μm , porosity 0.4, and tortuosity ϵ^{-1} , and is discretized into 10 finite volumes. The other key parameters used in Hybrid-MPET model of Li/CF_x-SVO can be seen in Table 3 and many reference Gomadam et al. [112],

Since CF_x-SVO is a hybrid electrode at both intra-particle and inter-particle scale, we adopt Eq. 4, 6 and 13, 16. Again, since $\rho_{\text{Ag}} = \frac{1}{3}\rho_{\text{SVO}}$, $\rho_{\text{V}} = \frac{2}{3}\rho_{\text{SVO}}$, we thus have,

$$\bar{c}_n^{\text{corr}} = \frac{\sum_{p_{\text{SVO}}=1}^{P_{\text{SVO}}} \rho_{\text{SVO}} V_{n,p_{\text{SVO}}} f_{n,\text{SVO}} \left(\frac{1}{3} \bar{c}_{n,p_{\text{SVO}},\text{Ag}} + \frac{2}{3} \bar{c}_{n,p_{\text{SVO}},\text{V}} \right) + \sum_{p_{\text{CF}}=1}^{P_{\text{CF}}} \rho_{\text{CF}} V_{n,p_{\text{CF}}} f_{n,\text{CF}} \bar{c}_{n,p_{\text{CF}}}}{\sum_{p_{\text{SVO}}=1}^{P_{\text{SVO}}} \rho_{\text{SVO}} V_{n,p_{\text{SVO}}} f_{n,\text{SVO}} + \sum_{p_{\text{CF}}=1}^{P_{\text{CF}}} \rho_{\text{CF}} V_{n,p_{\text{CF}}} f_{n,\text{CF}}} \quad (45)$$

Table 3: Geometric and materials properties used in simulating CF_x-SVO hybrid porous electrode

Parameter	Description	Unit	HB1	HB2	HB3	HB4
L	thickness	mm	2.1	2.1	2.1	2.6
ϵ	porosity	-	0.33	0.33	0.33	0.33
P_L	active solid volume fraction	-	0.88	0.85	0.84	0.85
τ	tortuosity	-	ϵ^{-1}	ϵ^{-1}	ϵ^{-1}	ϵ^{-1}
\tilde{Q}_{SVO}	capacity fraction of silicon	-	0.128	0.128	0.333	0.128
\tilde{Q}_{CF}	capacity fraction of graphite	-	0.872	0.872	0.667	0.872
Parameter	Description	Unit	Ag	V	CF _x	
R	particle radius	μm	$\mathcal{N}(1, 0.3)$		$\mathcal{N}(10, 0.5)$	
h	particle length	μm	20		-	
ρ	volumetric site density	mol m^{-3}	16107		32215	
α	symmetry coefficient	-	0.5		0.5	
k	rate constant	A m^{-2}	3.5×10^{-5}		1×10^{-3}	

$$R_n^{V,corr} = -(1 - \epsilon)P_L \left(\sum_{p_{SVO}=1}^{P_{SVO}} \tilde{V}_{n,p_{SVO}} \left(\frac{1}{3} \frac{\partial \bar{c}_{n,p_{SVO},Ag}}{\partial t} + \frac{2}{3} \frac{\partial \bar{c}_{n,p_{SVO},V}}{\partial t} \right) + \sum_{p_{CF}=1}^{P_{CF}} \tilde{V}_{n,p_{CF}} \frac{\partial \bar{c}_{n,p_{CF}}}{\partial t} \right) \quad (46)$$

where the corrected volume fractions are

$$\tilde{V}_{n,p_{SVO}} = \frac{V_{n,p_{SVO}} f_{n,SVO}}{\sum_{p_{SVO}=1}^{P_{SVO}} V_{n,p_{SVO}} f_{n,SVO} + \sum_{p_{CF}=1}^{P_{CF}} V_{n,p_{CF}} f_{n,CF}} \quad (47)$$

$$\tilde{V}_{n,p_{CF}} = \frac{V_{n,p_{CF}} f_{n,CF}}{\sum_{p_{SVO}=1}^{P_{SVO}} V_{n,p_{SVO}} f_{n,SVO} + \sum_{p_{CF}=1}^{P_{CF}} V_{n,p_{CF}} f_{n,CF}} \quad (48)$$

Supplementary Material

Supplementary Material is available with the electronic version of the article on the journal's website.

Competing interests

The authors declare no competing interests.

References

1. Arico, A. S., Bruce, P., Scrosati, B., Tarascon, J.-M. & Van Schalkwijk, W. Nanostructured materials for advanced energy conversion and storage devices. *Nature materials* **4**, 366–377 (2005).

2. Chu, S., Cui, Y. & Liu, N. The path towards sustainable energy. *Nature materials* **16**, 16–22 (2017).
3. Tarascon, J.-M. & Armand, M. Issues and challenges facing rechargeable lithium batteries. *nature* **414**, 359–367 (2001).
4. Andre, D. *et al.* Future generations of cathode materials: an automotive industry perspective. *Journal of Materials Chemistry A* **3**, 6709–6732 (2015).
5. Amine, K. *et al.* Advanced cathode materials for high-power applications. *Journal of power sources* **146**, 111–115 (2005).
6. Pillot, C. *The rechargeable battery market and main trends 2016–2025* in *Proceedings of the 33rd Annual International Battery Seminar & Exhibit, Fort Lauderdale, FL, USA* **20** (2017).
7. Chakraborty, A. *et al.* Layered cathode materials for lithium-ion batteries: review of computational studies on $\text{LiNi}_{1-x-y}\text{Co}_x\text{Mn}_y\text{O}_2$ and $\text{LiNi}_{1-x-y}\text{Co}_x\text{Al}_y\text{O}_2$. *Chemistry of Materials* **32**, 915–952 (2020).
8. Whittingham, M. S. Lithium batteries and cathode materials. *Chemical reviews* **104**, 4271–4302 (2004).
9. Thackeray, M. M. & Amine, K. Layered Li–Ni–Mn–Co oxide cathodes. *Nature Energy* **6**, 933–933 (2021).
10. Park, J. *et al.* Fictitious phase separation in Li layered oxides driven by electro-autocatalysis. *Nature Materials* **20**, 991–999 (2021).
11. Xia, Y., Zheng, J., Wang, C. & Gu, M. Designing principle for Ni-rich cathode materials with high energy density for practical applications. *Nano Energy* **49**, 434–452 (2018).
12. Radin, M. D. *et al.* Narrowing the gap between theoretical and practical capacities in Li-ion layered oxide cathode materials. *Advanced Energy Materials* **7**, 1602888 (2017).
13. Padhi, A. K., Nanjundaswamy, K. S. & Goodenough, J. B. Phospho-olivines as positive-electrode materials for rechargeable lithium batteries. *Journal of the electrochemical society* **144**, 1188 (1997).
14. Kang, B. & Ceder, G. Battery materials for ultrafast charging and discharging. *Nature* **458**, 190–193 (2009).
15. Guo, Y. *et al.* Li intercalation into graphite: direct optical imaging and Cahn–Hilliard reaction dynamics. *The journal of physical chemistry letters* **7**, 2151–2156 (2016).
16. Gao, T. *et al.* Interplay of lithium intercalation and plating on a single graphite particle. *Joule* **5**, 393–414 (2021).

17. Thomas-Alyea, K. E., Jung, C., Smith, R. B. & Bazant, M. Z. In situ observation and mathematical modeling of lithium distribution within graphite. *Journal of The Electrochemical Society* **164**, E3063 (2017).
18. Chikkannanavar, S. B., Bernardi, D. M. & Liu, L. A review of blended cathode materials for use in Li-ion batteries. *Journal of Power Sources* **248**, 91–100 (2014).
19. Schmidt, C. L. & Skarstad, P. M. The future of lithium and lithium-ion batteries in implantable medical devices. *Journal of power sources* **97**, 742–746 (2001).
20. Untereker, D. F. *et al.* Power sources and capacitors for pacemakers and implantable cardioverter-defibrillator. *Clinical Cardiac Pacing, Defibrillation and Resynchronization Therapy, 5th ed.; Ellenbogen, KA, Wilkoff, BL, Kay, GN, Lau, C.-P., Auricchio, A., Eds*, 251–269 (2016).
21. Gan, H., Rubino, R. S. & Takeuchi, E. S. Dual-chemistry cathode system for high-rate pulse applications. *Journal of power sources* **146**, 101–106 (2005).
22. Chen, K., Merritt, D. R., Howard, W. G., Schmidt, C. L. & Skarstad, P. M. Hybrid cathode lithium batteries for implantable medical applications. *Journal of power sources* **162**, 837–840 (2006).
23. Mond, H. G. & Freitag, G. The cardiac implantable electronic device power source: evolution and revolution. *Pacing and Clinical Electrophysiology* **37**, 1728–1745 (2014).
24. Chen, C.-H. *et al.* Development of experimental techniques for parameterization of multi-scale lithium-ion battery models. *Journal of The Electrochemical Society* **167**, 080534 (2020).
25. Jin, Y., Zhu, B., Lu, Z., Liu, N. & Zhu, J. Challenges and recent progress in the development of Si anodes for lithium-ion battery. *Advanced Energy Materials* **7**, 1700715 (2017).
26. Yoshio, M., Tsumura, T. & Dimov, N. Silicon/graphite composites as an anode material for lithium ion batteries. *Journal of power sources* **163**, 215–218 (2006).
27. Li, P., Kim, H., Myung, S.-T. & Sun, Y.-K. Diverting exploration of silicon anode into practical way: a review focused on silicon-graphite composite for lithium ion batteries. *Energy Storage Materials* **35**, 550–576 (2021).
28. Schmitt, J., Schindler, M. & Jossen, A. Change in the half-cell open-circuit potential curves of silicon-graphite and nickel-rich lithium nickel manganese cobalt oxide during cycle aging. *Journal of Power Sources* **506**, 230240 (2021).
29. Johnson, C. S., Li, N., Lefief, C., Vaughey, J. T. & Thackeray, M. M. Synthesis, characterization and electrochemistry of lithium battery electrodes: $x \text{ Li}_2\text{MnO}_3 \cdot (1-x) \text{ LiMn}_{0.333}\text{Ni}_{0.333}\text{Co}_{0.333}\text{O}_2$ ($0 \leq x \leq 0.7$). *Chemistry of Materials* **20**, 6095–6106 (2008).

30. Ai, W. *et al.* A composite electrode model for lithium-ion batteries with silicon/graphite negative electrodes. *Journal of Power Sources* **527**, 231142 (2022).
31. Cabana, J., Monconduit, L., Larcher, D. & Palacin, M. R. Beyond intercalation-based Li-ion batteries: the state of the art and challenges of electrode materials reacting through conversion reactions. *Advanced materials* **22**, E170–E192 (2010).
32. Wu, F. & Yushin, G. Conversion cathodes for rechargeable lithium and lithium-ion batteries. *Energy & Environmental Science* **10**, 435–459 (2017).
33. Heo, J. *et al.* Amorphous iron fluorosulfate as a high-capacity cathode utilizing combined intercalation and conversion reactions with unexpectedly high reversibility. *Nature Energy*, 1–10 (2022).
34. Thackeray, M. M. *et al.* Li₂MnO₃-stabilized LiMO₂ (M= Mn, Ni, Co) electrodes for lithium-ion batteries. *Journal of Materials chemistry* **17**, 3112–3125 (2007).
35. Kang, S.-H. & Thackeray, M. M. Enhancing the rate capability of high capacity xLi₂MnO₃·(1- x) LiMO₂ (M= Mn, Ni, Co) electrodes by Li–Ni–PO₄ treatment. *Electrochemistry Communications* **11**, 748–751 (2009).
36. Gallagher, K. G., Kang, S.-H., Park, S. U. & Han, S. Y. xLi₂MnO₃·(1- x) LiMO₂ blended with LiFePO₄ to achieve high energy density and pulse power capability. *Journal of Power Sources* **196**, 9702–9707 (2011).
37. Lee, K.-S., Myung, S.-T., Kim, D.-W. & Sun, Y.-K. AlF₃-coated LiCoO₂ and Li [Ni_{1/3}Co_{1/3}Mn_{1/3}] O₂ blend composite cathode for lithium ion batteries. *Journal of Power Sources* **196**, 6974–6977 (2011).
38. Albertus, P., Christensen, J. & Newman, J. Experiments on and modeling of positive electrodes with multiple active materials for lithium-ion batteries. *Journal of The Electrochemical Society* **156**, A606 (2009).
39. Kitao, H., Fujihara, T., Takeda, K., Nakanishi, N. & Nohma, T. High-temperature storage performance of Li-ion batteries using a mixture of Li-Mn spinel and Li-Ni-Co-Mn oxide as a positive electrode material. *Electrochemical and solid-state letters* **8**, A87 (2004).
40. Gao, J. & Manthiram, A. Eliminating the irreversible capacity loss of high capacity layered Li [Li_{0.2}Mn_{0.54}Ni_{0.13}Co_{0.13}] O₂ cathode by blending with other lithium insertion hosts. *Journal of Power Sources* **191**, 644–647 (2009).
41. Li, J. & Dahn, J. An in situ X-ray diffraction study of the reaction of Li with crystalline Si. *Journal of The Electrochemical Society* **154**, A156 (2007).

42. Liu, X. H. & Huang, J. Y. In situ TEM electrochemistry of anode materials in lithium ion batteries. *Energy & Environmental Science* **4**, 3844–3860 (2011).
43. Leising, R. A., Thiebolt III, W. C. & Takeuchi, E. S. Solid-state characterization of reduced silver vanadium oxide from the Li/SVO discharge reaction. *Inorganic Chemistry* **33**, 5733–5740 (1994).
44. Crespi, A., Skarstad, P. & Zandbergen, H. Characterization of silver vanadium oxide cathode material by high-resolution electron microscopy. *Journal of power sources* **54**, 68–71 (1995).
45. Ramasamy, R., Feger, C., Strange, T. & Popov, B. Discharge characteristics of silver vanadium oxide cathodes. *Journal of applied electrochemistry* **36**, 487–497 (2006).
46. Yu, G., Xie, X., Pan, L., Bao, Z. & Cui, Y. Hybrid nanostructured materials for high-performance electrochemical capacitors. *Nano Energy* **2**, 213–234 (2013).
47. Simon, P. & Gogotsi, Y. Materials for electrochemical capacitors. *Nature materials* **7**, 845–854 (2008).
48. Smith, R. B. & Bazant, M. Z. Multiphase porous electrode theory. *Journal of The Electrochemical Society* **164**, E3291 (2017).
49. Bai, P., Cogswell, D. A. & Bazant, M. Z. Suppression of phase separation in LiFePO₄ nanoparticles during battery discharge. *Nano letters* **11**, 4890–4896 (2011).
50. Ferguson, T. R. & Bazant, M. Z. Phase transformation dynamics in porous battery electrodes. *Electrochimica Acta* **146**, 89–97 (2014).
51. Harris, S. J. & Lu, P. Effects of Inhomogeneities-Nanoscale to Mesoscale-on the Durability of Li-Ion Batteries. *The Journal of Physical Chemistry C* **117**, 6481–6492 (2013).
52. Li, Y. *et al.* Current-induced transition from particle-by-particle to concurrent intercalation in phase-separating battery electrodes. *Nature materials* **13**, 1149–1156 (2014).
53. Chueh, W. C. *et al.* Intercalation pathway in many-particle LiFePO₄ electrode revealed by nanoscale state-of-charge mapping. *Nano letters* **13**, 866–872 (2013).
54. Bazant, M. *et al.* Learning heterogeneous reaction kinetics from X-ray movies pixel-by-pixel (2022).
55. Agrawal, S. & Bai, P. Dynamic interplay between phase transformation instabilities and reaction heterogeneities in particulate intercalation electrodes. *Cell Reports Physical Science* **3**, 100854 (2022).
56. Agrawal, S. & Bai, P. Operando electrochemical kinetics in particulate porous electrodes by quantifying the mesoscale spatiotemporal heterogeneities. *Advanced Energy Materials* **11**, 2003344 (2021).
57. Ferguson, T. R. & Bazant, M. Z. Nonequilibrium thermodynamics of porous electrodes. *Journal of The Electrochemical Society* **159**, A1967 (2012).

58. Torchio, M., Magni, L., Gopaluni, R. B., Braatz, R. D. & Raimondo, D. M. Lionsimba: a matlab framework based on a finite volume model suitable for li-ion battery design, simulation, and control. *Journal of The Electrochemical Society* **163**, A1192 (2016).
59. Sulzer, V., Marquis, S. G., Timms, R., Robinson, M. & Chapman, S. J. Python battery mathematical modelling (PyBaMM). *Journal of Open Research Software* **9** (2021).
60. Berliner, M. D., Cogswell, D. A., Bazant, M. Z. & Braatz, R. D. Methods—PETLION: Open-source software for millisecond-scale porous electrode theory-based lithium-ion battery simulations. *Journal of The Electrochemical Society* **168**, 090504 (2021).
61. Albertus, P. & Newman, J. Introduction to dualfoil 5.0. *University of California Berkeley, Berkeley, CA, Tech. Rep* (2007).
62. Newman, J. & Tiedemann, W. Porous-electrode theory with battery applications. *AIChE Journal* **21**, 25–41 (1975).
63. Newman, J. S. & Tobias, C. W. Theoretical analysis of current distribution in porous electrodes. *Journal of The Electrochemical Society* **109**, 1183 (1962).
64. Doyle, M., Fuller, T. F. & Newman, J. Modeling of galvanostatic charge and discharge of the lithium/polymer/insertion cell. *Journal of the Electrochemical society* **140**, 1526 (1993).
65. Fuller, T. F., Doyle, M. & Newman, J. Simulation and optimization of the dual lithium ion insertion cell. *Journal of the electrochemical society* **141**, 1 (1994).
66. Doyle, M., Newman, J., Gozdz, A. S., Schmutz, C. N. & Tarascon, J.-M. Comparison of modeling predictions with experimental data from plastic lithium ion cells. *Journal of the Electrochemical Society* **143**, 1890 (1996).
67. Bazant, M. Z. Theory of chemical kinetics and charge transfer based on nonequilibrium thermodynamics. *Accounts of chemical research* **46**, 1144–1160 (2013).
68. Bazant, M. Z. Thermodynamic stability of driven open systems and control of phase separation by electro-autocatalysis. *Faraday discussions* **199**, 423–463 (2017).
69. Bazant, M. Z. Phase-field theory of ion intercalation kinetics. *arXiv preprint arXiv:1208.1587* (2012).
70. Singh, G. K., Ceder, G. & Bazant, M. Z. Intercalation dynamics in rechargeable battery materials: General theory and phase-transformation waves in LiFePO₄. *Electrochimica Acta* **53**, 7599–7613 (2008).
71. Burch, D., Singh, G., Ceder, G. & Bazant, M. Z. Phase-transformation wave dynamics in LiFePO₄ in *Solid State Phenomena* **139** (2008), 95–100.

72. Bazant, M. Z., Kilic, M. S., Storey, B. D. & Ajdari, A. Towards an understanding of induced-charge electrokinetics at large applied voltages in concentrated solutions. *Advances in colloid and interface science* **152**, 48–88 (2009).
73. Burch, D. & Bazant, M. Z. Size-dependent spinodal and miscibility gaps for intercalation in nanoparticles. *Nano letters* **9**, 3795–3800 (2009).
74. Van der Ven, A., Bhattacharya, J. & Belak, A. A. Understanding Li diffusion in Li-intercalation compounds. *Accounts of chemical research* **46**, 1216–1225 (2013).
75. Srinivasan, V. & Newman, J. Discharge model for the lithium iron-phosphate electrode. *Journal of the Electrochemical Society* **151**, A1517 (2004).
76. Heß, M. & Novák, P. Shrinking annuli mechanism and stage-dependent rate capability of thin-layer graphite electrodes for lithium-ion batteries. *Electrochimica Acta* **106**, 149–158 (2013).
77. Cahn, J. W. & Hilliard, J. E. Free energy of a nonuniform system. I. Interfacial free energy. *The Journal of chemical physics* **28**, 258–267 (1958).
78. Cahn, J. W. On spinodal decomposition. *Acta metallurgica* **9**, 795–801 (1961).
79. Cogswell, D. A. & Bazant, M. Z. Coherency strain and the kinetics of phase separation in LiFePO₄ nanoparticles. *ACS nano* **6**, 2215–2225 (2012).
80. Cogswell, D. A. & Bazant, M. Z. Theory of coherent nucleation in phase-separating nanoparticles. *Nano letters* **13**, 3036–3041 (2013).
81. Li, Y. *et al.* Fluid-enhanced surface diffusion controls intraparticle phase transformations. *Nature materials* **17**, 915–922 (2018).
82. Newman, J. & Balsara, N. P. *Electrochemical systems* (John Wiley & Sons, 2021).
83. Bard, A. J., Faulkner, L. R., *et al.* Fundamentals and applications. *Electrochemical methods* **2**, 580–632 (2001).
84. Dreyer, W., Gohlke, C. & Müller, R. A new perspective on the electron transfer: recovering the Butler–Volmer equation in non-equilibrium thermodynamics. *Physical Chemistry Chemical Physics* **18**, 24966–24983 (2016).
85. Heubner, C., Schneider, M. & Michaelis, A. Investigation of charge transfer kinetics of Li-Intercalation in LiFePO₄. *Journal of Power Sources* **288**, 115–120 (2015).
86. Thomas, K. E., Newman, J. & Darling, R. M. *Mathematical modeling of lithium batteries* (Springer, 2002).

87. Zhao, H. & Bazant, M. Z. Population dynamics of driven autocatalytic reactive mixtures. *Physical Review E* **100**, 012144 (2019).
88. Kganyago, K. & Ngoepe, P. Structural and electronic properties of lithium intercalated graphite LiC₆. *Physical Review B* **68**, 205111 (2003).
89. Ohzuku, T., Iwakoshi, Y. & Sawai, K. Formation of lithium-graphite intercalation compounds in nonaqueous electrolytes and their application as a negative electrode for a lithium ion (shuttlecock) cell. *Journal of The Electrochemical Society* **140**, 2490 (1993).
90. Harris, S. J., Timmons, A., Baker, D. R. & Monroe, C. Direct in situ measurements of Li transport in Li-ion battery negative electrodes. *Chemical Physics Letters* **485**, 265–274 (2010).
91. Jo, Y. N. *et al.* Si-graphite composites as anode materials for lithium secondary batteries. *Journal of Power Sources* **195**, 6031–6036 (2010).
92. Müller, S. *et al.* Quantification and modeling of mechanical degradation in lithium-ion batteries based on nanoscale imaging. *Nature communications* **9**, 2340 (2018).
93. Verbrugge, M., Baker, D. & Xiao, X. Formulation for the treatment of multiple electrochemical reactions and associated speciation for the lithium-silicon electrode. *Journal of The Electrochemical Society* **163**, A262 (2015).
94. Lu, B. *et al.* Voltage hysteresis of lithium ion batteries caused by mechanical stress. *Physical Chemistry Chemical Physics* **18**, 4721–4727 (2016).
95. Wang, M. & Xiao, X. Investigation of the chemo-mechanical coupling in lithiation/delithiation of amorphous Si through simulations of Si thin films and Si nanospheres. *Journal of Power Sources* **326**, 365–376 (2016).
96. Chen, L. *et al.* A phase-field model coupled with large elasto-plastic deformation: application to lithiated silicon electrodes. *Journal of The Electrochemical Society* **161**, F3164 (2014).
97. Son, I. H. *et al.* Silicon carbide-free graphene growth on silicon for lithium-ion battery with high volumetric energy density. *Nature communications* **6**, 7393 (2015).
98. Liu, N. *et al.* A pomegranate-inspired nanoscale design for large-volume-change lithium battery anodes. *Nature nanotechnology* **9**, 187–192 (2014).
99. Hu, Y.-S. *et al.* Superior storage performance of a Si@ SiO_x/C nanocomposite as anode material for lithium-ion batteries. *Angewandte Chemie International Edition* **47**, 1645–1649 (2008).
100. Gu, M. *et al.* In situ TEM study of lithiation behavior of silicon nanoparticles attached to and embedded in a carbon matrix. *Acs Nano* **6**, 8439–8447 (2012).

101. Popp, H., GLANZ, G., HAMID, R. & ZHANG, N. *Benchmark, ageing and Ante-Mortem of SOTA CCylindrical lithium-ion cells in 14th international A3PS conference on eco-mobility* (2019).
102. Popp, H. *et al.* Ante-mortem analysis, electrical, thermal, and ageing testing of state-of-the-art cylindrical lithium-ion cells. *Elektrotech. Informationstechnik* **137**, 169–176 (2020).
103. Smith, R. B., Khoo, E. & Bazant, M. Z. Intercalation kinetics in multiphase-layered materials. *The Journal of Physical Chemistry C* **121**, 12505–12523 (2017).
104. Ai, W., Kraft, L., Sturm, J., Jossen, A. & Wu, B. Electrochemical thermal-mechanical modelling of stress inhomogeneity in lithium-ion pouch cells. *Journal of The Electrochemical Society* **167**, 013512 (2020).
105. Lory, P. *et al.* Probing silicon lithiation in silicon-carbon blended anodes with a multi-scale porous electrode model. *Journal of The Electrochemical Society* **167**, 120506 (2020).
106. Zandbergen, H., Crespi, A., Skarstad, P. & Vente, J. Two structures of Ag₂-xV₄O₁₁, determined by high resolution electron microscopy. *Journal of Solid State Chemistry* **110**, 167–175 (1994).
107. Crespi, A., Schmidt, C., Norton, J., Chen, K. & Skarstad, P. Modeling and characterization of the resistance of lithium/SVO batteries for implantable cardioverter defibrillators. *Journal of the Electrochemical Society* **148**, A30 (2001).
108. Leifer, N. *et al.* Nuclear magnetic resonance and X-ray absorption spectroscopic studies of lithium insertion in silver vanadium oxide cathodes. *Journal of the Electrochemical Society* **154**, A500 (2007).
109. Sauvage, F. *et al.* Structural and transport evolution in the Li_xAg₂V₄O₁₁ system. *Journal of Power Sources* **195**, 1195–1201 (2010).
110. Takeuchi, K. J., Marschilok, A. C., Davis, S. M., Leising, R. A. & Takeuchi, E. S. Silver vanadium oxides and related battery applications. *Coordination Chemistry Reviews* **219**, 283–310 (2001).
111. Onoda, M. & Kanbe, K. Crystal structure and electronic properties of the Ag₂V₄O₁₁ insertion electrode. *Journal of Physics: Condensed Matter* **13**, 6675 (2001).
112. Gomadam, P. M. *et al.* Modeling Li/ CF x-SVO Hybrid-Cathode Batteries. *Journal of the Electrochemical Society* **154**, A1058 (2007).
113. West, K. & Crespi, A. Lithium insertion into silver vanadium oxide, Ag₂V₄O₁₁. *Journal of power sources* **54**, 334–337 (1995).
114. Garcia-Alvarado, F. & Tarascon, J. Lithium intercalation in Ag₂V₄O₁₁. *Solid State Ionics* **73**, 247–254 (1994).

115. Sasaki, T., Ukyo, Y. & Novák, P. Memory effect in a lithium-ion battery. *Nature materials* **12**, 569–575 (2013).
116. Farkhondeh, M., Pritzker, M., Fowler, M., Safari, M. & Delacourt, C. Mesoscopic modeling of Li insertion in phase-separating electrode materials: application to lithium iron phosphate. *Physical Chemistry Chemical Physics* **16**, 22555–22565 (2014).
117. Delmas, C., Maccario, M., Croguennec, L., Le Cras, F. & Weill, F. Lithium deintercalation in LiFePO₄ nanoparticles via a domino-cascade model. *Nature materials* **7**, 665–671 (2008).
118. Brunetti, G. *et al.* Confirmation of the domino-cascade model by LiFePO₄/FePO₄ precession electron diffraction. *Chemistry of Materials* **23**, 4515–4524 (2011).
119. Robert, D. *et al.* Multiscale phase mapping of LiFePO₄-based electrodes by transmission electron microscopy and electron forward scattering diffraction. *ACS nano* **7**, 10887–10894 (2013).
120. Jacobsen, T., Zachau-Christiansen, B., West, K. & Atlung, S. Li insertion in Cu₂TiS₂ spinels. *Electrochimica acta* **34**, 1473–1477 (1989).
121. McKinnon, W. & Dahn, J. Salting-out in intercalation compounds: removing copper from Cu₃Mo₆S₈ by intercalating lithium. *Solid state communications* **52**, 245–248 (1984).
122. Takahashi, M., Tobishima, S., Takei, K. & Sakurai, Y. Characterization of LiFePO₄ as the cathode material for rechargeable lithium batteries. *Journal of Power Sources* **97**, 508–511 (2001).
123. Dreyer, W. *et al.* The thermodynamic origin of hysteresis in insertion batteries. *Nature materials* **9**, 448–453 (2010).
124. Dreyer, W., Gohlke, C. & Herrmann, M. Hysteresis and phase transition in many-particle storage systems. *Continuum Mechanics and Thermodynamics* **23**, 211–231 (2011).
125. Dreyer, W., Müller, I. & Strehlow, P. A study of equilibria of interconnected balloons. *The Quarterly Journal of Mechanics and Applied Mathematics* **35**, 419–440 (1982).
126. John, W. On spinodal decomposition Sur la decomposition spinodale Über die umsetzung an der spinodalen. *Acta Metall* **9**, 795–801 (1961).
127. Allen, J., Jow, T. & Wolfenstine, J. Analysis of the FePO₄ to LiFePO₄ phase transition. *Journal of Solid State Electrochemistry* **12**, 1031–1033 (2008).
128. Allen, J. L., Jow, T. R. & Wolfenstine, J. Kinetic study of the electrochemical FePO₄ to LiFePO₄ phase transition. *Chemistry of materials* **19**, 2108–2111 (2007).

129. Oyama, G., Yamada, Y., Natsui, R.-i., Nishimura, S.-i. & Yamada, A. Kinetics of nucleation and growth in two-phase electrochemical reaction of $\text{Li} \times \text{FePO}_4$. *The Journal of Physical Chemistry C* **116**, 7306–7311 (2012).
130. Zhang, Q., Takeuchi, K. J., Takeuchi, E. S. & Marschilok, A. C. Progress towards high-power Li/CF_x batteries: electrode architectures using carbon nanotubes with CF_x . *Physical Chemistry Chemical Physics* **17**, 22504–22518 (2015).
131. Liu, Y. *et al.* A brief review for fluorinated carbon: synthesis, properties and applications. *Nanotechnology Reviews* **8**, 573–586 (2019).
132. Tiedemann, W. Electrochemical behavior of the fluorographite electrode in nonaqueous media. *Journal of The Electrochemical Society* **121**, 1308 (1974).
133. Davis, S., Takeuchi, E. S., Tiedemann, W. & Newman, J. Simulation of the $\text{Li}-\text{CF}_x$ System. *Journal of the Electrochemical Society* **154**, A477 (2007).
134. Grisolia, M., Rozier, P. & Benoit, M. Density functional theory investigations of the structural and electronic properties of $\text{Ag}_2\text{V}_4\text{O}_{11}$. *Physical Review B* **83**, 165111 (2011).
135. Pinson, M. B. & Bazant, M. Z. Theory of SEI formation in rechargeable batteries: capacity fade, accelerated aging and lifetime prediction. *Journal of the Electrochemical Society* **160**, A243 (2012).
136. Jana, A. *et al.* Physics-based, reduced order degradation model of lithium-ion batteries. *Journal of Power Sources* **545**, 231900 (2022).
137. Dose, W. *et al.* Capacity fade in high energy silicon-graphite electrodes for lithium-ion batteries. *Chemical Communications* **54**, 3586–3589 (2018).
138. Dhillon, S., Hernández, G., Wagner, N. P., Svensson, A. M. & Brandell, D. Modelling capacity fade in silicon-graphite composite electrodes for lithium-ion batteries. *Electrochimica Acta* **377**, 138067 (2021).
139. Zhuang, D. & Bazant, M. Z. Theory of layered-oxide cathode degradation in Li-ion batteries by oxidation-induced cation disorder. *Journal of The Electrochemical Society* **169**, 100536 (2022).
140. Finegan, D. P. *et al.* Spatial dynamics of lithiation and lithium plating during high-rate operation of graphite electrodes. *Energy & Environmental Science* **13**, 2570–2584 (2020).
141. Liang, Q. *Hybrid-MPET: an open-source simulation software for hybrid electrode batteries* at <https://github.com/HarryQL/Hybrid-MPET>. 2023.
142. Rowlinson, J. S. Translation of JD van der Waals “The thermodynamik theory of capillarity under the hypothesis of a continuous variation of density”. *Journal of Statistical Physics* **20**, 197–200 (1979).

143. Liu, B. *et al.* Multiphysics coupled computational model for commercialized Si/graphite composite anode. *Journal of Power Sources* **450**, 227667 (2020).